

HiCIAO Performance Report for SEEDS

- Final Report -

2009.9.14, 24(revised)

HiCIAO team, SEEDS team

SUMMARY

HiCIAO is a new high-contrast instrument for the Subaru telescope. HiCIAO is used in conjunction with the new adaptive optics (AO) system (AO188/LGSAO188) at the Infrared Nasmyth platform. HiCIAO can combine coronagraphic techniques with conventional direct imaging, polarization differential imaging, or spectral differential imaging (DI/SDI/PDI) modes. The basic concept of simultaneous differential imaging is to split up the image into two or more images, and then use either different planes of polarization, or different spectral filter band-passes, or both, to produce a signal that distinguishes objects near a star (such as planets or disks) from residual speckles of the bright central star. A new observing technique called angular differential imaging (ADI) is also incorporated, and can be combined with the above DI/PDI/SDI modes. The instrument started development in 2004 and obtained its first light with AO188 in 2008 Dec. Eleven nights were allocated for commissioning, of which 8 were clear and usable for tests. The combination of HiCIAO and AO188 is to be used for the first Subaru Strategic Observing Program (SSOP) for the Subaru Strategic Explorations of Exoplanets and Disks Survey (SEEDS).

This document concisely describes the current status of HiCIAO and its performance obtained both in the laboratory and at the telescope during its commission runs for the performance verification review.

Coronagraph masks (0.3", 0.6" diameter) are regularly used during the commissioning with a spider-pattern suppressing Lyot stop. We have measured 5σ 1hr on-sky contrasts of $\sim 10^{-5.6}$ at $r=1''$ (all modes), $\sim 10^{-4.6}$ at $r=0.5''$ (all modes), $\sim 10^{-4.2}$ at $r=0.3''$ (SDI/PDI), and finally $10^{-3.9}$ at as close as $r=0.15''$ (SDI/PDI). For comparison, the CIAO+AO36 typical mask sizes was $>0.6''$ and the K band contrast was $10^{-4.3}$ at $r=1.2''$. Thus, the HiCIAO contrast is more than 1 order of magnitude better than the CIAO contrast. In fact all three planets around HR8799 are easily detected in only ~ 9 min at H band. The measured values on-sky are consistent with those of the simulations in the HiCIAO CDR document calculated in the same method. Instrument performances as an IR camera are consistent with the design except for a higher background in the K band. However, the instrument is contrast-limited and the H band is mainly used in the SEEDS survey; thus this is not a problem.

AO polarimetry at Nasmyth platform is complicated by the large instrumental polarizations caused by the telescope tertiary mirror and mirrors within AO. Nonetheless, these can be corrected with appropriate models for mirrors and telescope image rotation, enabling polarimetry very close to the central source. We have demonstrated a dual-beam polarimetry accuracy of 1% level with HiCIAO+AO188 (the PDI mode). This is the first polarimetry on the Subaru Nasmyth platform.

Regarding the "real" observation procedures, HiCIAO is well interfaced with SOSS and the AO188 software; their combination is as smooth as or even better than the previous CIAO+AO36 case. We have enough man powers for the long term SEEDS observations as several SEEDS members are experienced in operating SOSS and HiCIAO.

Therefore, we conclude that all DI, SDI, PDI, ADI modes and their certain combinations are now available and ready for the SEEDS survey.

Contents and Main Contributors

1. Introduction of HiCIAO and laboratory test summary.....	3
1.1 HiCIAO introduction	
1.2 Performance evaluation in the laboratory	
2. Observing software and general observing procedures.....	8
2.1 Observation interfaces	
2.2 Observation procedure and overhead	
2.3 Observation man powers	
2.4 Summary	
3. Camera performance.....	11
3.1 Summary	
3.2 Detector performance	
3.3 Optical performance	
4. Direct Imaging (DI) mode performance.....	19
4.1 Observations	
4.2 Data reduction	
4.3 AO performance with HiCIAO	
4.4 Contrast with self-subtraction	
4.5 DI mode summary	
5. Spectral Differential Imaging (SDI) mode performance.....	23
5.1 Observations	
5.2 Data reduction	
5.3 Contrast	
6. Angular Differential Imaging (ADI) mode performance.....	28
6.1 Observations	
6.2 Data reduction	
6.3 Contrast	
6.4 HR8799 demo	
7. Polarization Differential Imaging (PDI) mode performance.....	34
7.1 Observations	
7.2 Data reduction	
7.3 Contrast in intensity	
7.4 Unpolarized stars	
8. Aperture polarimetry performance and extended object.....	37
8.1 Unpolarized stars	
8.2 Polarized standard	
8.3 Extended objects	
9. Impact of performance on planet and disk detection.....	40
Appendix 1. Contrast summary table and figure.....	43
Appendix 2. Distortion details.....	44

Main contributors

Suzuki, R., Kudo, T., Kandori, R., Kusakabe, N., Morino, J., Hodapp, K., Goto, M., Thalmann, C., McElwain, M., Carson, J., Hashimoto, J., Suto, H., Matsuo, T., Egner, S., Tamura, M.

Acknowledgements

We thank the AO188 team and other SEEDS people who supported/joined the HiCIAO commissioning runs, in particular, Hayano, Y., Egner, S., Minowa, Y., Pyo, T. S., Kuzuhara, M.

1. Introduction of HiCIAO and laboratory test summary

HiCIAO is a high contrast instrument for the 8.2 m Subaru Telescope. The instrument is specially designed to search for exoplanets and protoplanetary or debris disks. HiCIAO is given a sharp point spread function (PSF) by the new adaptive optics system for the Subaru Telescope (AO188; Hayano et al. 2008) whose Strehl ratio is measured to be 0.4 in the H-band and 0.6 in the K-band. Besides the quality PSF, HiCIAO is implementing a classical Lyot coronagraph and various types of differential imaging techniques to achieve the high contrast. HiCIAO's observing modes include a spectral differential imaging mode (SDI mode), a polarimetric differential imaging mode (PDI mode), and a normal imaging mode (DI mode). The angular differential imaging mode (ADI mode) is also available in combination with other modes. A pixel scale of $0.''01 \text{ pixel}^{-1}$ gives a corresponding field of view of $20'' \times 20''$ in the DI mode, $20'' \times 10''$ in the PDI mode, and $5'' \times 5''$ in the SDI mode, respectively. The expected contrasts in the SDI mode are $10^{-5.5}$ at $1.0''$ separation from a central star. Specifications are summarized in Table 1.1.

Table 1.1 Specification Table

Wavelength	0.85 – 2.50 μm
Observing modes	DI, PDI, SDI, + ADI
	With or without occulting mask
Spatial resolution	$0.''03$ (J), $0.''04$ (H), $0.''06$ (K)
Strehl ratio	0.2 (J), 0.3 (H), 0.5 (K)
Field of view	$20'' \times 20''$ (DI)
	$20'' \times 10''$ (PDI)
	$5'' \times 5''$ (SDI)
Contrast	$10^{-5.5}$ at $1''$, 10^{-4} at $0.''1^*$
Pixel scale	$0.''01 \text{ pixel}^{-1}$
Occulting mask	Semi-transmissive, hard edged
Lyot stop	Hard edged, continuous rotation, spider blocking
Filters	Y, J, H, K (DI and PDI)
	CH_4 , [FeII], H_2 (SDI)
	ND

* SDI with coronagraph

The HiCIAO project was started in 2004. The fabrication was done mainly at the laboratory of the University of Hawai'i. The laboratory experiments have been conducted to characterize detector performance, imaging performance, and coronagraphic performance. The instrument was brought up to the summit of Mauna Kea in November 2008, and the first-light observation followed in December 2008.

1.1 HiCIAO introduction

1.1.1 Hardware layout

HiCIAO hardware is comprised of three modules: the warm coronagraph module, the cryogenic infrared camera module, and the instrument support frame module (see Figure 1.1). The warm coronagraph module is attached to the AO optical bench to prevent image motion due to vibration. The cryogenic infrared camera module is located on the instrument support frame which stands by itself. Figure 1.2 shows the optical layout of HiCIAO. The HiCIAO optics consist of a collimator and a camera section. The collimator and the camera sections are accommodated in the warm coronagraph module and the cryogenic infrared camera module, respectively. The optics are designed in a simple configuration to reduce possible ghost imaging, scattered light on the lens surfaces, and wavefront errors. There has also been a special effort to achieve a low non-common path wavefront error, which is critical to the high-contrast imaging with differential imaging techniques using a Wollaston prism.

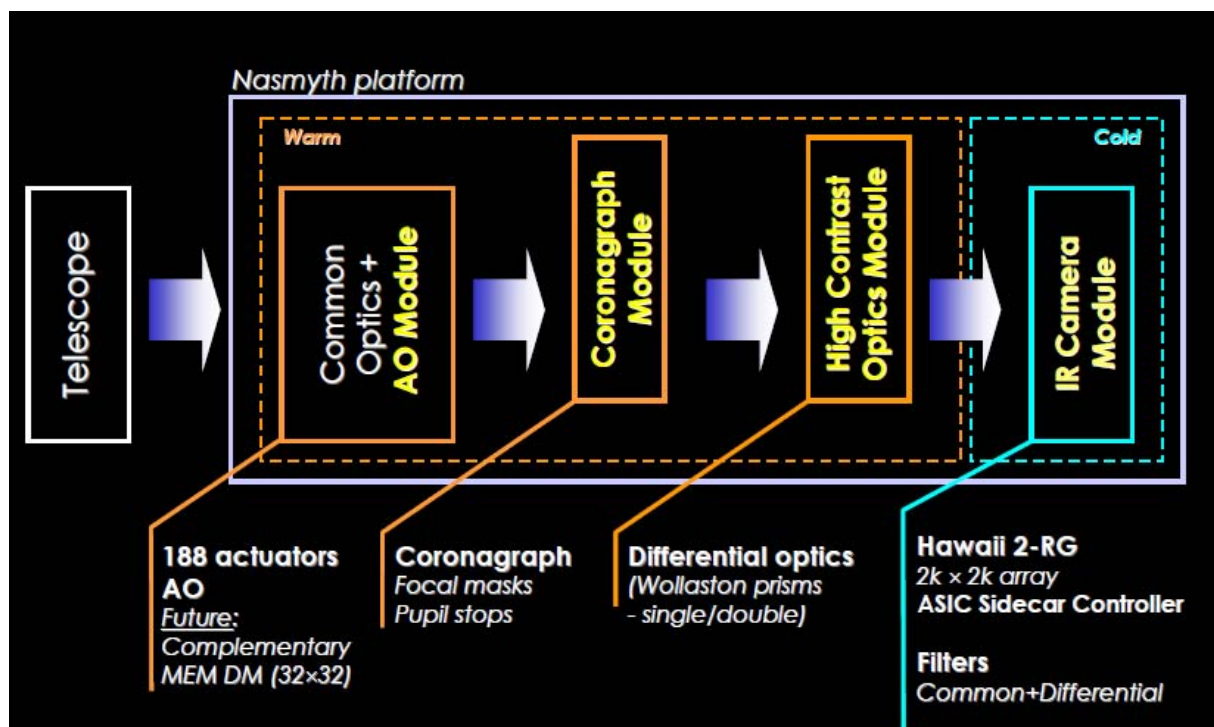
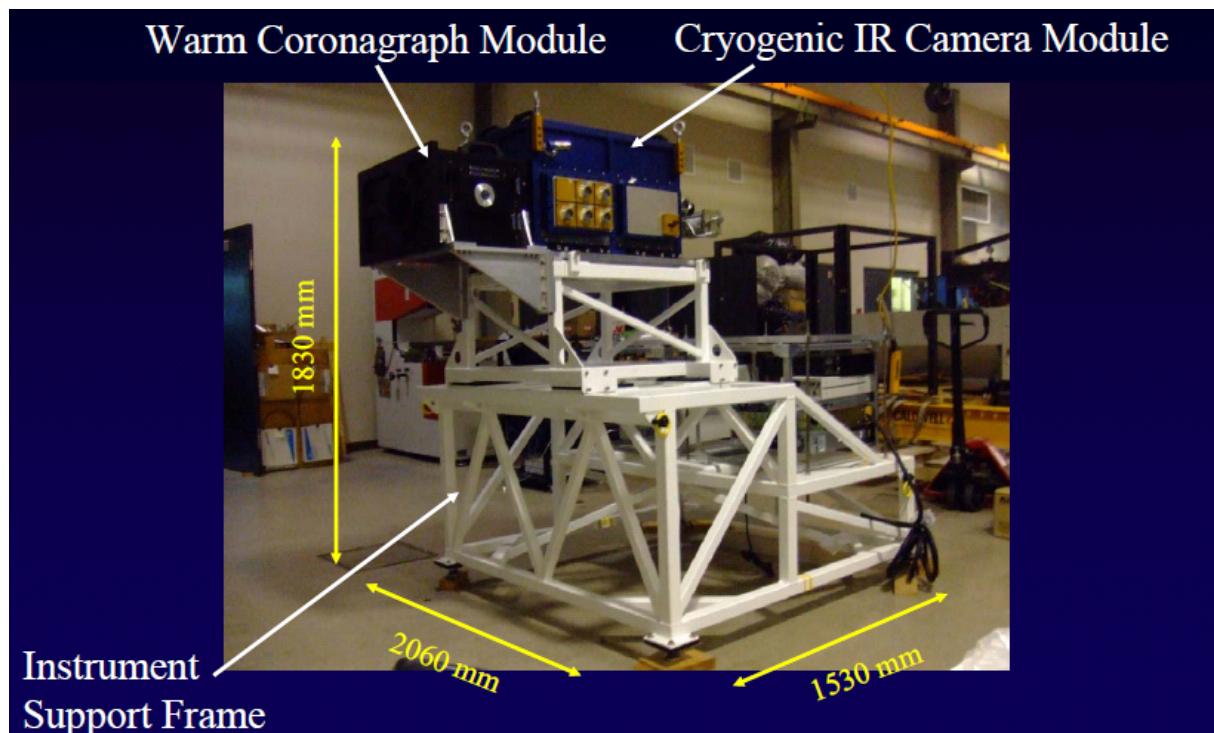


Figure 1.1: (top) Whole picture of the HiCIAO instrument. A black box and a blue box on the top are the warm coronagraph module and the cryogenic camera module, respectively. (bottom) Schematic diagram of the HiCIAO system.

Optics Layout

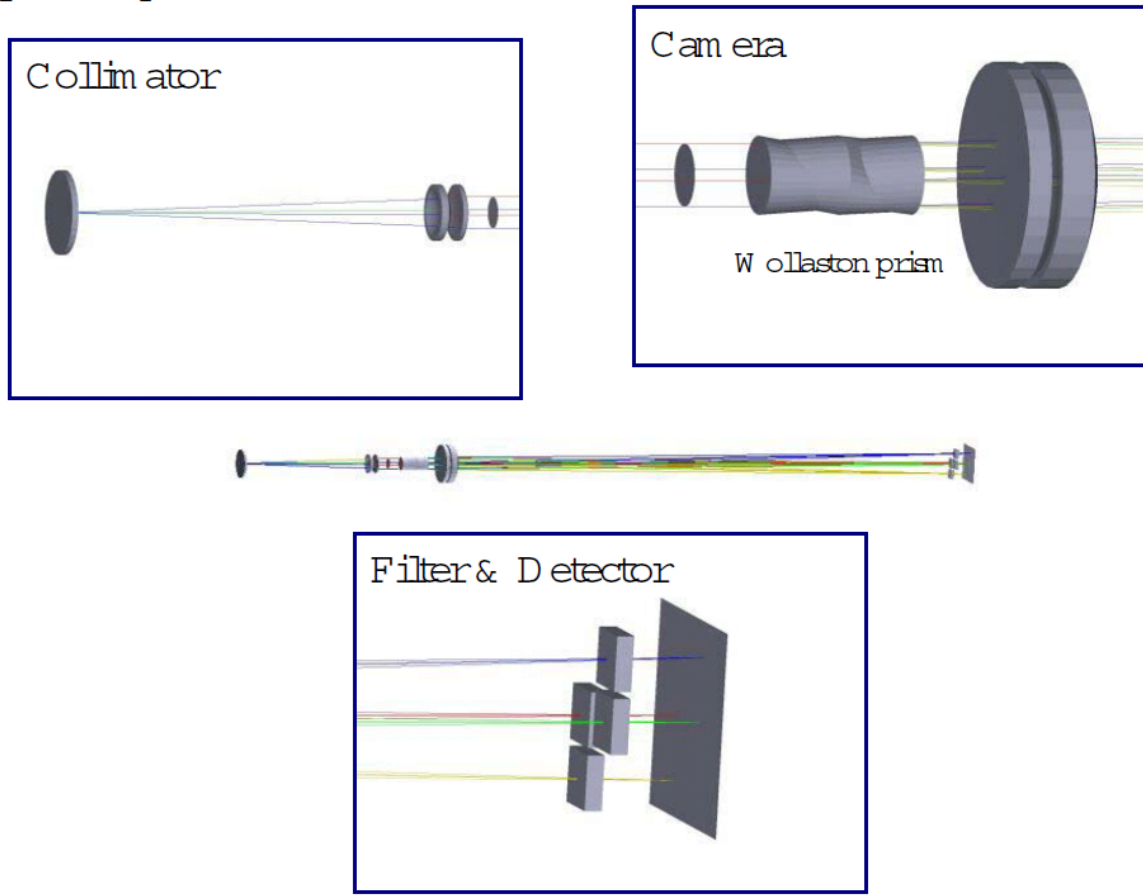


Figure 1.2: Optical layout of HiCIAO (center). Closer looks at three portions are also shown.

1.1.2 Warm coronagraph module

The warm coronagraph module contains a compensator, a shutter, field masks, occulting masks, the collimator lenses, the Lyot stop, and the Wollaston prisms. As a default configuration, we adopt a classical Lyot coronagraph with a hard-edged occulting mask and Lyot stop. A semi-transmissive and circular occulting mask is deposited on the plano surface of a field lens using a lithographic technique. The Lyot stop is an aluminum piece fabricated by EDM (Electrical Discharge Machining) and its surface is painted black to reduce ghost images. The Lyot stop resembles the telescope pupil image, but it is shaped to hide diffracted light from the telescope. There are two Wollaston prisms made of YLF which split the light into two (in the PDI mode) and four (in the SDI mode). As most optical components in this module are mounted on motorized stages, precise alignment between the telescope and the instrument is possible, which is essential for the coronagraph instrument.

Since the HiCIAO coronagraph optics are warm, the control mechanisms are more precise than the cooled mechanisms. High precision warm mechanisms include the continuous rotation of the Lyot stop that produces a clean PSF unaffected by the large support spiders for the Subaru secondary mirror.

1.1.3 Cryogenic infrared camera module

The cryogenic infrared camera module consists of the camera lenses, three filter wheels, and the detector housing (Figure 1.3). The camera lens also acts as a vacuum window of the cryostat. The filter wheels and the detector housing are inside the cryostat, and kept at 77 K and 60 K respectively using a mechanical cooler and heaters. The three filter wheels accommodate filters for the DI and the PDI mode, special narrow-band filter sets for the SDI mode, and pupil viewer optics. We use the SIDECAR ASIC controller, the JADE2 card, and a

Windows PC to operate the HAWAII-2RG detector array. A dedicated flat cable is used between the detector and the ASIC and between the ASIC and the JADE2, respectively. The JADE2 communicates with the control PC through a USB cable. The ASIC is mounted on the detector housing because of the short flat cable to minimize the pick up noise, while the JADE2 is attached to the outside wall of the cryostat. The ASIC is actively cooled to 100 K by the mechanical cooler.

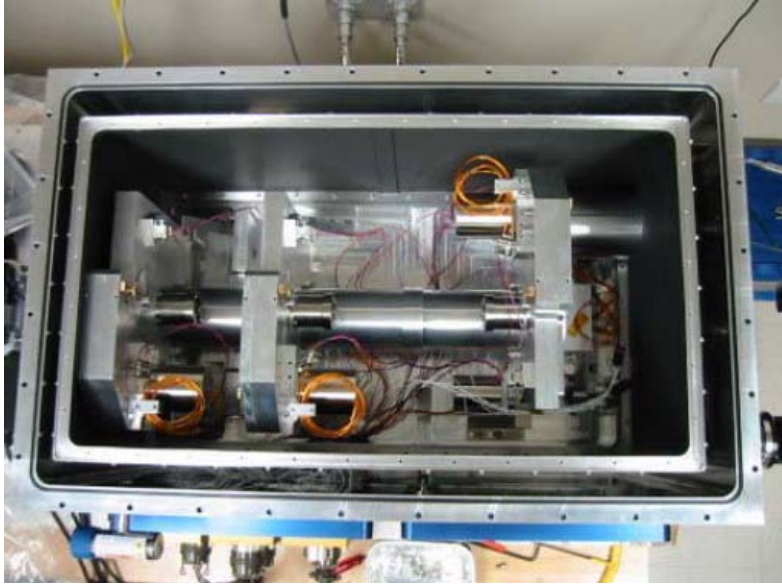


Figure 1.3: Inside the cryogenic infrared camera module.

1.2 Performance evaluation in the laboratory

In this section, we describe some results from the performance evaluation of the instrument in the laboratory. Since the main results in this document are on sky data, the description here is brief.

1.2.1 Optics performance

The Strehl ratio of the instrument itself is measured with a pinhole. Figure 1.4 compares radial profiles of the simulated and measured PSFs in the H-band, whose images are also shown in Figure 1.4. The Strehl ratio of the instrument is almost 1, which is expected from the design.

1.2.2 Coronagraph performance

Contrast performance is estimated in the laboratory using optics simulating AO188 and the telescope. The experimental conditions are chosen to simulate an observation with H=7 stars with an exposure time of 1 hour, which will be a typical observation in the SEEDS project. Figure 1.4 shows the contrast profile with a 0."6 mask as a function of distance from the mask center. The contrast is found to be $10^{-5.5}$ at 1" separation, which satisfies the specification. However, we note that the contrast is limited by the readout noise at 1" separation because the Strehl ratio of the experiment is very high ($SR \sim 1$).

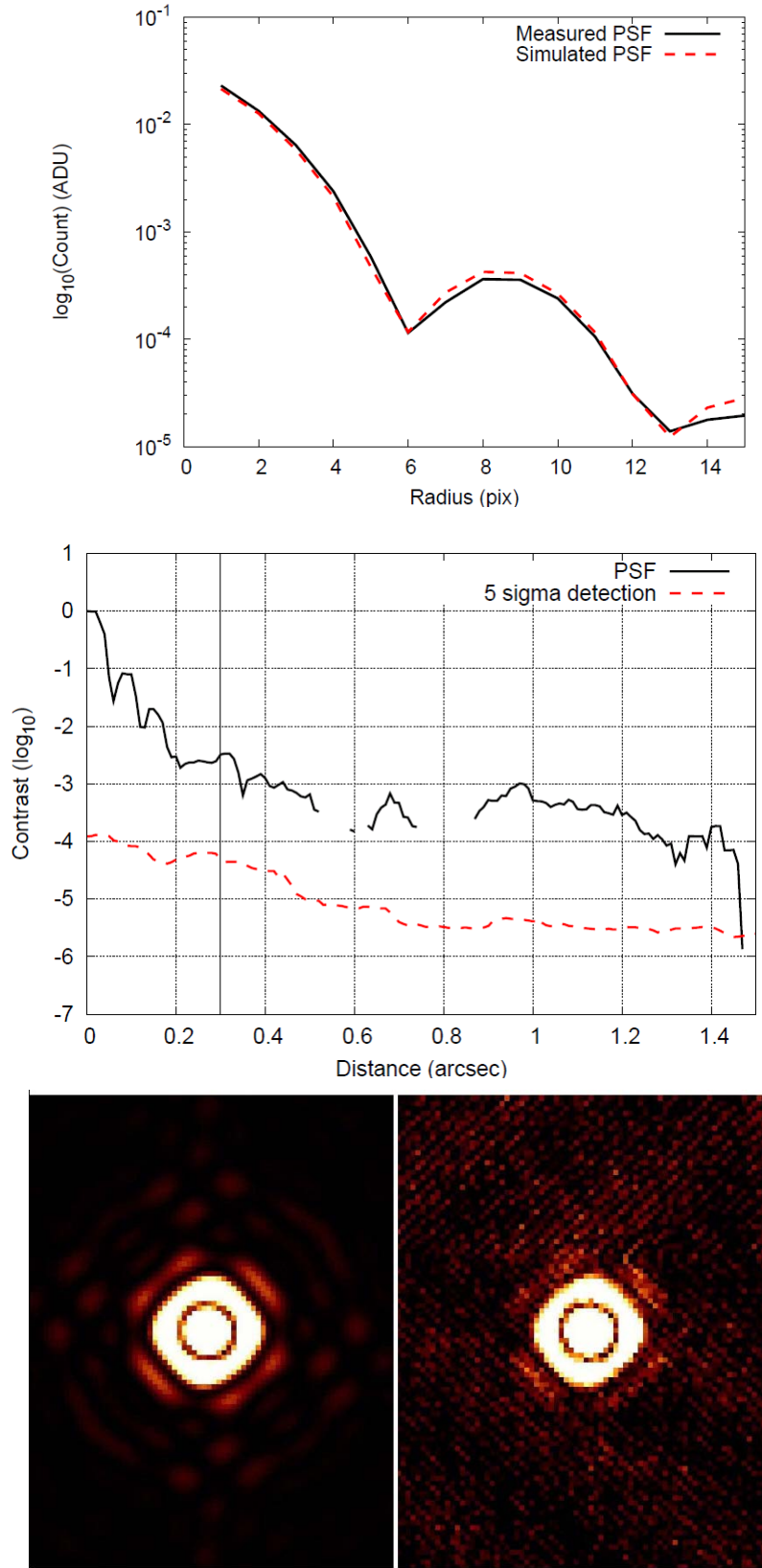


Figure 1.4: (*top*) Radial profile of the simulated (dashed line) and measured (solid line) PSFs. (*middle*) Radial profile of the contrast with the 0."6 mask. The PSF without the mask and 5σ detection level are shown as a solid and dashed line, respectively. (*bottom*) Simulated PSF (left) and measured PSF of HiCIAO itself (right).

2. Observing software and general observing procedures

2.1 Observation interfaces

There are two interfaces for the observers to conduct observations with HiCIAO. One is using GUI running locally in the control PC (OBCP), and the other is through the Subaru Observation Software System (SOSS) (see Figure 2.1). Both interfaces are used in the observation as described in §2.2. In case of the SOSS, abstract commands have been prepared for each fundamental observation procedure such as SETUPFIELD, SETUPOBE, GETOBJECT, etc. Observers can program their observation sequence using the abstract commands in a form of "ope file" like other Subaru instruments. Operation of AO is either with an SOSS command launcher or a command line interface, but it should be done only by AO operators or experienced observers. On the other hand, the GUI is a quicker and more flexible way to control the instrument when something unexpected happens or when observers want to change the observation method on the fly. The GUI includes a motion control interface, a detector control interface, a status monitor, an exposure time calculator, an image viewer, and an interface for pupil alignment and object alignment (See Figure 2.2). The status monitor, the exposure time calculator, and the interface for alignments are only available with the GUI. The SOSS/GUI interface is also available for the waveplate unit.

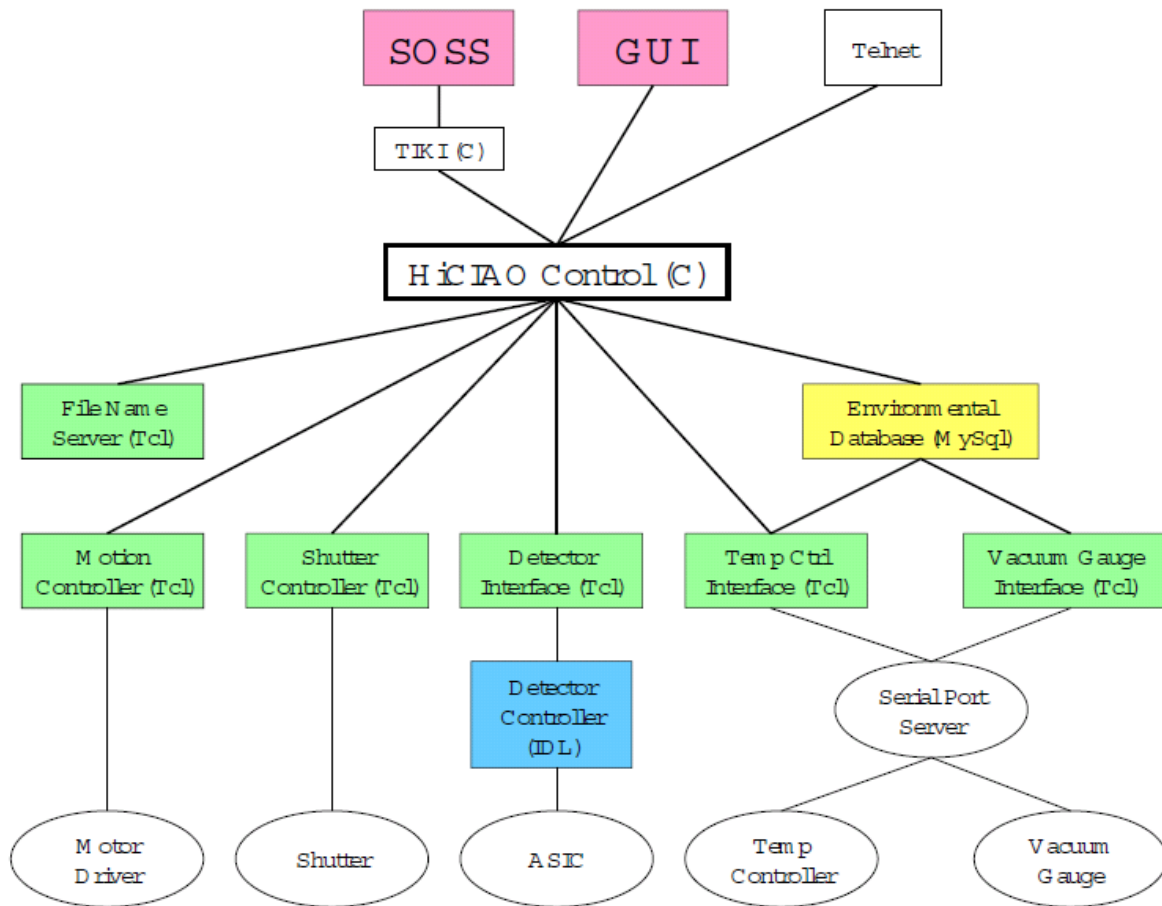


Figure 2.1: HiCIAO software diagram. Three boxes on the top are user interfaces. Rectangle and oval means software and hardware object, respectively. Thick solid line represents software communication, while thin solid line represents hardware connection.

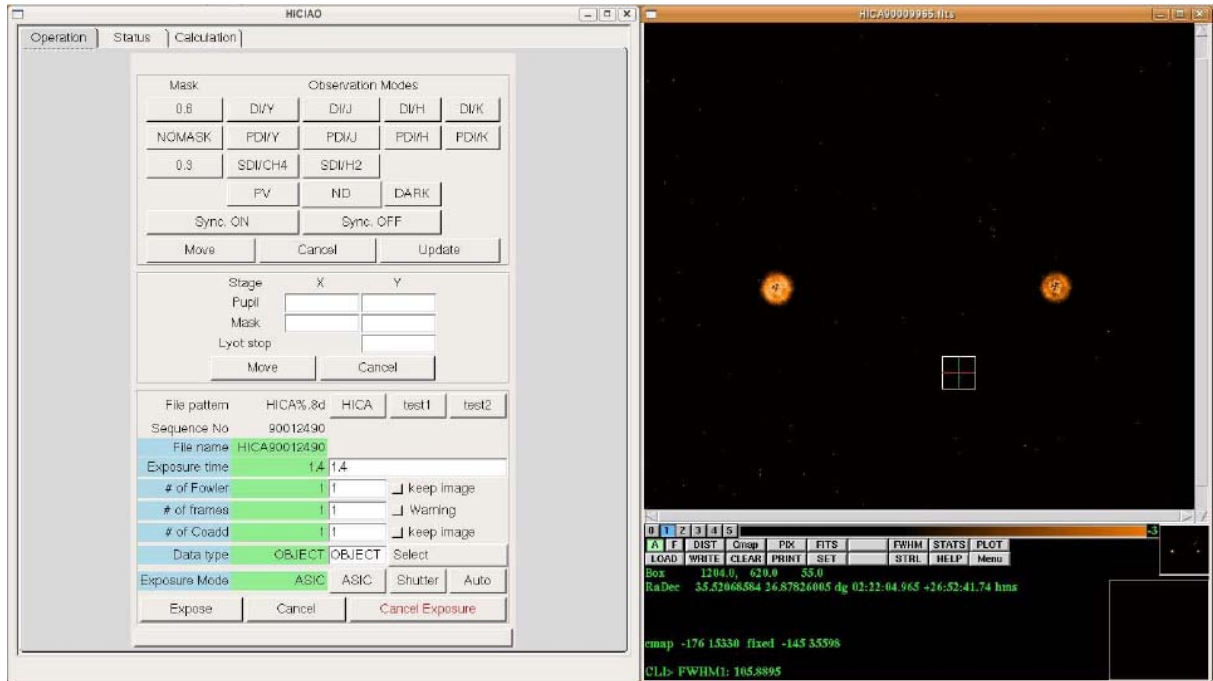


Figure 2.2: HiCIAO control, status, and calculation GUI (left) and image viewer (right).

2.2 Observation procedures and overhead

The followings are procedures of a typical coronagraph observation in the SEEDS observations with associated interface and overhead time.

No.	Procedure	Interface	Overhead time
1.	Target acquisition and observing mode set up	SOSS/ope file	
2.	Check field	SOSS/ope file	
3.	Set AO point	SOSS/launcher	2 min
4.	Move object to the center of FOV	SOSS/launcher	1 min
5.	Adjust pupil position on the Lyot stop	GUI	~2 min
6.	AO parameter tuning	AO operator+GUI	< 10 min
7.	Obtain PSF reference if necessary	SOSS/ope file	
8.	Adjust object position on the occulting mask	SOSS/launcher+GUI	~3 min
9.	Start science observation	SOSS/ope file	
10.	Obtain PSF reference if necessary	SOSS/ope file	

The target acquisition time has been greatly improved after a telescope pointing analysis was done in July 2007. The target object can be always found in a small HiCIAO's FOV at the first glance, compared to the previous situation where we spent more than 20 minutes to find the object at every target acquisition. Overhead time in taking one frame is 6.8 seconds: 2 seconds is for the OBCP to collect necessary information for the exposure and to transfer the file, and 4.8 seconds is for the detector control system to set up the exposure, read out the pixels, and generate a frame. Observers can reduce the former 2 seconds by coadding multiple frames. All the overhead time listed above and written here are close to the minimum values, and we believe that they will not hamper efficient operation of the SEEDS observations.

2.3 Observation man powers

As of writing, two people are necessary except the observation PI to conduct the observation smoothly: an SOSS and AO operator, and a HiCIAO operator (assuming that the PI can write the observation log). Running the observation with fewer people is important in the SEEDS

project as it will be allocated fairly long consecutive nights. Currently, five members in the HiCIAO team can operate SOSS/GUI, and a few are learning AO operation. We will be able to conduct the SEEDS observations with a telescope/instrument operator and SEEDS members (note that some AO team members are in the SEEDS project).

2.4 Summary

The SOSS and GUI interfaces provide all functionality necessary for the SEEDS observations. They have been improved in the past engineering observations, and the improvement results in acceptable amount of overhead and the minimum number of people necessary for the observation. Although we will keep improving the software based on feedbacks from the observers, we believe that the observation software sets are ready to start the SEEDS observations.

3. Camera performance

3.1 Summary

Table 3.1 is a summary of the camera performances described below.

Table 3.1 Summary of camera performance

Items	Measured values	Design values
Detector gain	$1.60 \text{ e}^- \text{ ADU}^{-1}$	-
Readout noise	15 e^- (or less; see text)	15 e^-
Dark current	$0.104 \text{ e}^- \text{ s}^{-1}$	$0.088 \text{ e}^- \text{ s}^{-1}$
Overhead	6.8 s	-
Throughput (DI)* ¹	0.09(J)/0.11(H)/0.16(Ks)	0.09(J)/0.11(H)/0.14(Ks)
Distortion (DI)* ²	0.4 pix (rms) in central 5"x5" 0.8 pix (rms) in 20"x20"	-
Pixel scale	9.53 milliarcsec pix ⁻¹	9.60 milliarcsec pix ⁻¹
Flat accuracy	0.05 mag (rms) w/ stars 0.006 mag in different flats	-
Ghost (DI)	Pupil-like ghost (see text)	-
Ghost (SDI)	Point-like ghost (see text)	-
Background brightness* ³	13.2(H)/10.1(Ks) mag arcsec ⁻²	13.4(H)/12.6(Ks) mag arcsec ⁻²
Limiting magnitudes* ⁴ (1hr, 5 σ , 0.075" aperture)	24.52(J)/24.08(H)/22.54(Ks) 24.05(J)/23.69(H)/22.17(Ks)	24.28(J)/24.16(H)/23.84(Ks)
Strehl ratio	0.4(H)/0.6(K)	0.3(H)/0.5(K) from AO* ⁵

*¹: Including AO, with 50% HiCIAO stop.

*²: The values are based on the on-sky data and detailed models in Appendix 2.

*³: Design values are with reflective Lyot stop, while measured values with non reflective one.

*⁴: Upper values are without Lyot stop, while lower values are with 50% Lyot stop. The design values in the CDR are specified without Lyot stop (as a simple camera).

*⁵: The values of 0.7(H)/0.8(K) in the CDR document assumed the 2 Stroke approach that is not yet implemented.

We believe that overall camera performance is ready for the start of the SEEDS survey because all of the measured values are consistent with the expected values and there are no critical parameters for conducting the survey.

3.2 Detector performance

3.2.1 Raw image

Figure 3.1 (left) shows a dark image as an example of the raw image. There are two significant features in the raw image due to the current characteristics of the ASIC readout: horizontal stripes occurring at 64 pixel interval and vertical bandings whose interval is random in each image. The horizontal stripes are said to be due to a bias instability caused by temperature fluctuations in the detector/ASIC. In order to remove the stripe patterns, extra pixels called "reference pixels" are provided along the edges of the detector that have the same characteristics as rest of the pixels, but are not light sensitive. This "reference pixel subtraction" removes the horizontal stripes almost completely. It also works for the vertical bandings, but some residuals persist, as shown in Figure 3.1.

In order to improve the horizontal and the vertical pattern subtraction, we can use a part of the image that has virtually no light signals. As the horizontal stripes only differ in their amplitudes and the vertical bandings are common among 32 horizontal stripes, we can pick up some of the 32 horizontal stripes, make a template pattern out of them, and subtract the

template from each horizontal stripe after appropriate scaling. This “stripe subtraction” method works much better than the reference pixel subtraction as shown in Figure 3.1. However, we note that this method is only applicable under a certain condition where we have some stripes which accept virtually no light signals. For example, in the SDI mode with a methane filter set, it will always work because there are one stripe each at the top and the bottom of the image which are outside of a field stop. On the other hand, the method will not work in the DI mode for objects with an extended flux over the entire detector.

In summary, although some careful calibration is necessary as the first step of data reduction, compared with the previous conventional IR array readout, these de-stripping procedures will work in most cases and should not be a problem in the SEEDS survey.

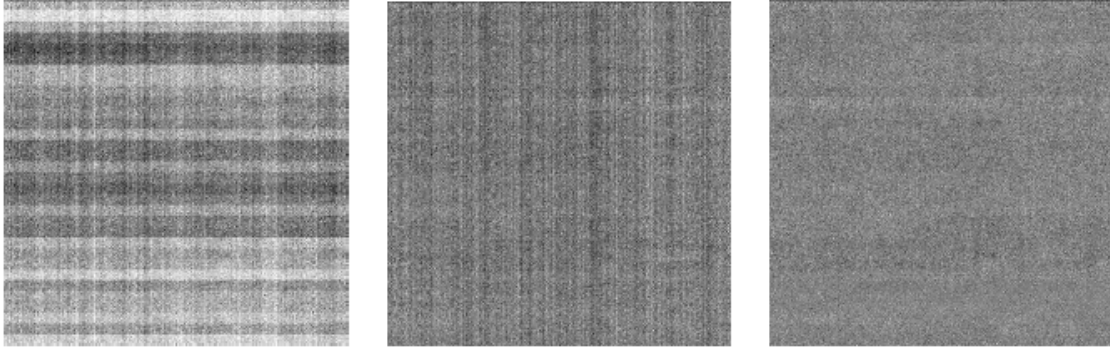


Figure 3.1: (left) Raw image (dark image), (center) Image after the reference pixel subtraction, (right) Image after the stripe subtraction.

3.2.2 Gain

Detector gain in $e^- \text{ADU}^{-1}$ is derived by a photon transfer curve which is expressed in a form,

$$N_{\text{total}}^2 = N_{\text{read}}^2 + \frac{S}{g} \quad (3)$$

where N_{total} is total noise, N_{read} readout noise, and S signal, all in units of analog-to-digital units (ADU). An aluminum plate at room temperature is used as a light source in the Ks band. Two images are obtained at each count level, and subtraction of the two images is used to calculate N^2_{total} . Figure 3.2 shows the obtained photon transfer curve. We sample several portions of the image (40×40 pixels each) for the statistics, and obtain the gain of $1.60 e^- \text{ADU}^{-1}$. The gain might sound low, considering the readout noise is $15 e^-$ (as described in § 3.2.3). We are using the lower gain because a higher gain caused a higher readout noise. We think that the detector electronics (especially amplifier) can be optimized for a certain gain value.

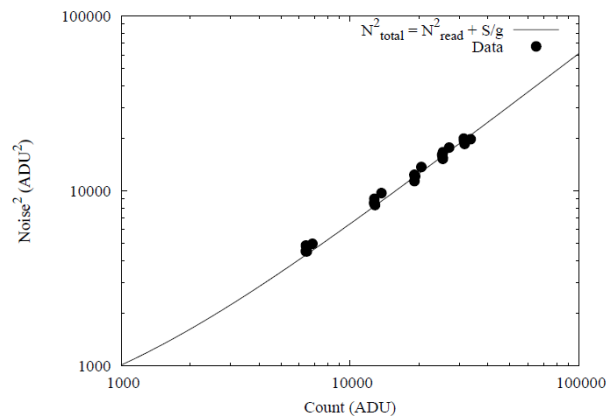


Figure 3.2: Photon transfer curve. Filled circles are data points, and a solid line is a best fit result on the data.

3.2.3 Readout noise

Readout noise of the detector is measured using two dark images subtracted from each other. The measured readout noise of 15 e^- is consistent with specification. This value is fine for the high contrast imaging case because our region of interest is inside the speckle dominated regime rather than the detector noise limit. We can also effectively reduce the noise by the software "binning" or "smoothing" (see §3.3.7).

We have tried a multiple sampling method to reduce the readout noise by a factor of $1/\sqrt{N}$ where N is the number of sampling. Figure 3.3 shows the readout noise as a function of the number of sampling. We can see a trend that the readout noise decreases as a function of $1/\sqrt{N}$ at least to $N=16$. Since exposure time of the coronagraph observation with fainter objects will be longer than a few minutes, multiple sampling is worth doing even at a cost of additional overhead time of $2.8 \times N\text{ s}$.

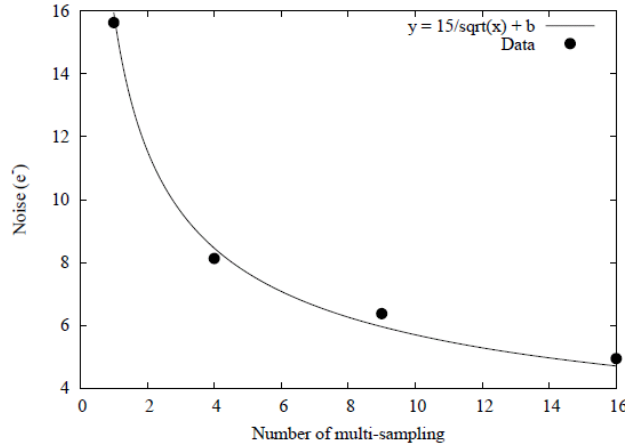


Figure 3.3: Readout noise as a function of the number of sampling.

3.2.4 Dark current

Dark current is measured by taking dark images with different exposure times. A black-painted aluminum plate at 77 K was placed in front of the detector. The detector was operated at 60 K. The dark current is $0.104\text{ e}^- \text{ s}^{-1}$ which is consistent with a result that the detector vendor reported.

3.2.5 Hot and bad pixels

The HiCIAO detector array has less than 1% bad/hot pixels. Since most bad/hot pixels are isolated, the current number of bad/hot pixels can be handled in the image analysis and is totally acceptable. However, it is noted that we have confirmed that the number of hot pixels can be reduced by adjusting operating temperature of the detector. We might have a fewer hot pixels by the SEEDS observations.

3.2.6 Expected overhead in SEEDS observations

Since objects in the SEEDS target list are typically bright, overhead time in detector readout has a big impact on observation efficiency. The overhead time was 22 s in the past engineering observations. After reviewing each process of the readout procedure and taking measures for some of them, we were able to reduce the overhead time to 6.8 s.

Although the overheads for target pointing and the AO setting are sometimes ~ 10 minutes each, this can be minimized when we plan the SEEDS targets to sort with similar coordinates and similar magnitudes. In this case, we expect this overhead is ~ 10 minutes in total.

On the other hand, the overhead for the integration time is limited by the readout overhead. For example, we expect the typical integration time to be 10-20 s for DI or ADI+DI modes. In this case, of the 1hr allocation for each target, 10 minutes are for pre-exposure overhead,

28-36 minutes are integration. In contrast, the typical integration time for SDI or SDI+ADI modes are up to tens of minutes and thus the readout-overhead is negligible, so ~50 minutes can be devoted for integration.

This overhead is comparable to or less than that of CIAO+AO36, and acceptable for the SEEDS survey.

3.3 Optics performance

3.3.1 Throughput

Throughput is calculated using the following formula,

$$\gamma = \frac{C_{\text{obj}}g}{F_{\lambda,\text{obj}}A_{\text{tel}}\Delta\lambda} \quad (1)$$

where C_{obj} is a count rate of an object in ADU s^{-1} , g the detector gain in $\text{e}^- \text{ADU}^{-1}$, $F_{\lambda,\text{obj}}$ the photon flux of the object in $\text{photon s}^{-1} \text{cm}^{-2} \mu\text{m}^{-1}$, A_{tel} the effective area of the telescope in cm^2 , and $\Delta\lambda$ the passband width of a filter in μm . A total of 11 stars have been observed to derive the throughput: three stars are from the UKIRT Faint Standard Star Catalog and eight stars were observed as a part of coronagraph tests. The measured throughputs are 0.09 in the J band, 0.11 in the H band, and 0.16 in the Ks band. The measured values are consisted with the expected numbers as shown in Table 3.1.

3.3.2 Distortion (see Appendix 2 for on-sky data with detailed models)

Here we derive two distortions separately: distortion of the HiCIAO optics only, and distortion of the optical system including the telescope, AO, and HiCIAO.

The distortion of the HiCIAO optics is measured from an image of a pinhole grid located at the AO focal plane. The pinhole grid is accurate enough for this purpose (error is $\sim 1 \mu\text{m}$) because it is made using a lithographic process. A third order polynomial is used when we correlate the measured and the predicted coordinate of the pinholes to calculate a Seidel's distortion coefficient. The measured coefficient is consistent with the design within 3% and the amount of distortion is about 0.25% at the edge of the image (Figure 3.4).

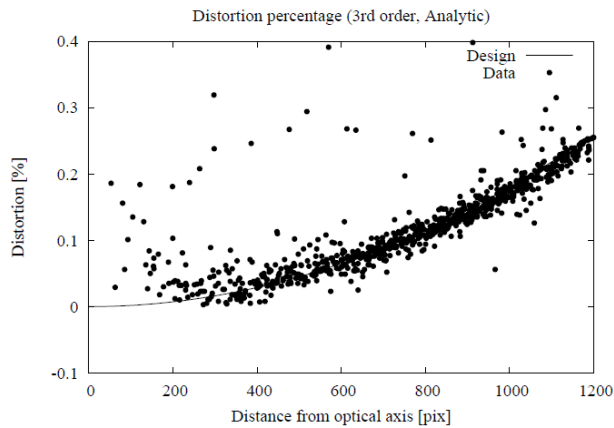


Figure 3.4: Amount of distortion in the HiCIAO optics as a function of distance from the optical axis. The data are with only HiCIAO optics (not including AO and the telescope). Filled circles are data points and a solid line is a prediction from the design.

The distortion of the optical system is measured from images of globular clusters (M5 and M15). Detail of the analysis and the result are described in Appendix 2. The HST images of these clusters with the distortion correction are assumed to be distortion-free and serve as

reference frames. A third order polynomial is used to describe the distortion pattern, and it is fitted to the data which is difference of object coordinates between the HiCIAO and the HST images. The accuracy of distortion correction is 0.78 pixels or 7.4 mas in 20" x 20" FOV. The result is satisfactory for our purpose which is, for example, a proper motion test of possible companions around a star. We note that the correction accuracy becomes 0.2 pixels in 10" x 10" FOV when the images at different position angles are compared (this is the case for image registration in the ADI mode). The same analysis is planned for the PDI and SDI modes.

3.3.3 Pixel scale

Pixel scale can be derived at the same time as the distortion. Thus we obtain the pixel scale of the HiCIAO optics only and the pixel scale of the optical system.

The pixel scale of the HiCIAO optics is measured to be 9.53 milliarcsec pix^{-1} which is consistent with the design (9.60 milliarcsec pix^{-1}).

On the other hand, in the distortion correction algorithm that we have used this time, the pixel scale of the optical system is a free parameter and, within some range, can be chosen freely. As written in Appendix A2, we just chose a pixel scale of 9.5 milliarcsec pix^{-1} . Since we have obtained the distortion map with good quality, measurement of the accurate pixel scale using reference objects such as astrometric binaries or satellites of the planets in Solar system will be the next step.

3.3.4 Flat accuracy

We compare three kinds of illumination sources for flat fielding (dome flat light, calibration light, and twilight) to see which gives the best photometric accuracy over the FOV. We observed a star with a nine-dithered pattern on the image, and uniformity of the photometry of the nine images is compared among the different illumination sources. We do not see significant difference among the three illumination sources, however, all three give a photometric scatter of 0.05 mag (rms), which is not sufficient for our purposes. We have not located a cause of the problem yet.

On the other hand, the flatness with dome/twilight is much better (0.6% in the whole array; see § 4.2.1).

3.3.5 Ghost

Ghost image is investigated both in the laboratory and on the sky. In the laboratory using a light source with high Strehl ratio ($\text{SR} \sim 1$), no ghost image brighter than 10^{-6} of the ghost source is found outside of a 0."5 radius when the occulting mask is used in the DI mode. On the sky, there are two occasions where the ghost image has been found so far in the course of contrast analysis and ghost measurement analysis: one is an observation in the DI mode without occulting mask, and the other is an observation in the SDI mode (see Figure 3.5). The ghost image in the DI mode is a pupil-like ghost. The contrast is $10^{-5.6} \text{ pix}^{-1}$ of the ghost source and the size is 260 pix in radius. On the other hand, the ghost image in the SDI mode is a point-like ghost. It is generated by a double-bounce reflection at the detector surface and the surface of the differential filter. The ghost can be found in all four channels of the SDI image. The location is either 0."31 or 0."67 from the ghost source depending on the channel, and the contrast is $10^{-4.3}$ of the ghost source. Since these ghosts are predictable, it is not a problem for the SEEDS companion survey.

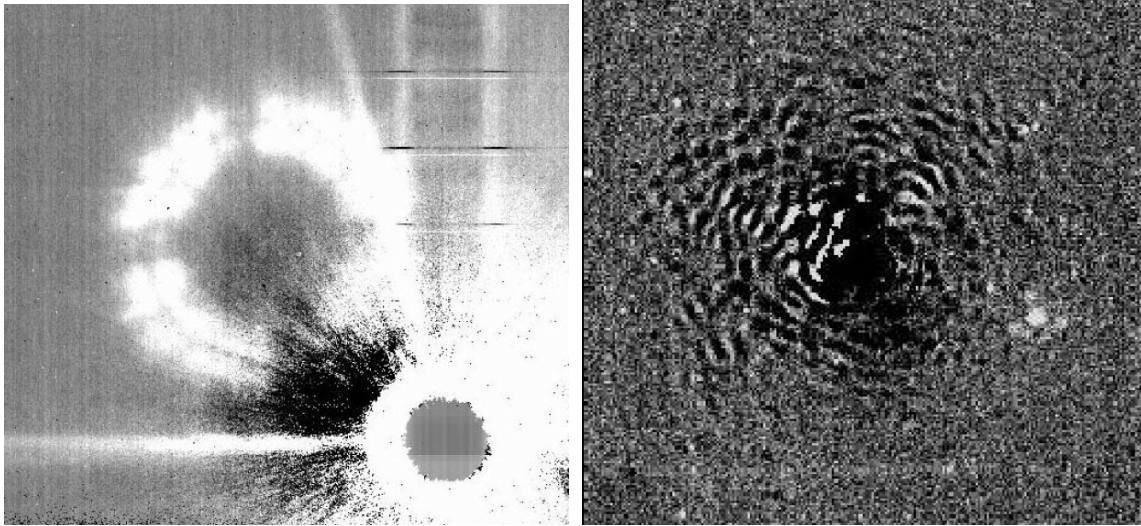


Figure 3.5: (left) Ghost image in DI mode. (right) Ghost image in SDI mode.

3.3.6 Background brightness

Background brightness is calculated using the following formula,

$$m_{bg} = -2.5 \log\left(\frac{C_{bg} g \gamma h c}{A_{tel} \lambda \Delta \lambda \theta^2}\right) + m_0 - 10 \quad (2)$$

where C_{bg} is a count rate of background regions in ADU s^{-1} , g the detector gain in $\text{e}^- \text{ADU}^{-1}$, the throughput obtained in § 3.3.1, h the Plank constant in erg s , c the light velocity in cm s^{-1} , λ center wavelength of the filter transmission in μm , θ the pixel scale in arcsec pix^{-1} , and m_0 the zero point of the Vega magnitude calculated from the throughput obtained in § 3.3.1. Measured background brightness is 13.2 mag arcsec⁻² in the H band and 9.3 and 10.1 mag arcsec⁻² in the Ks band with and without a shutter, respectively. The H band value is consistent with typical sky brightness at Mauna Kea, while the Ks band gives a higher value because the detector sees the HiCIAO foreoptics and AO optics which work at room temperature. We checked that the dominant radiation source in the Ks band is the Lyot stop when the shutter is not used, and guess that the shutter was the brightest source when the shutter was used. The background brightness in the Ks band without shutter is roughly consistent with the calculation assuming that the Lyot stop is at temperature measured on the AO optical bench. Lower background could be achieved by using a reflective Lyot stop, but a serious ghost image is expected as we observed in the laboratory. As for the shutter, we are looking for a new shutter which dissipates less energy than the current one. Alternative is using ND filters instead of the shutter for bright objects as we did in the August run. In any case, it is noted that the high background in the K band is not a problem for the SEEDS project in which we use H band, and that the higher K band background is part of the original HiCIAO design.

3.3.7 Sensitivity

Limiting magnitudes are calculated using the measured values described above. The measured limiting magnitudes with 1 hour exposure, 5 σ level, and 0."075 aperture as an IR camera (no Lyot stop) are 24.52, 24.08, and 22.54 in the J, H, K bands, respectively. These are roughly consistent with the designed values in the CDR document except for the K band and also consistent with the limiting magnitudes of IR cameras on the 8-m telescopes with similar AO (NIRI, NAOS). However, it should be noted that there are some uncertainties in the aperture corrections and "accurate" limiting magnitudes are not always meaningful. Furthermore, the coronagraphic observations stress higher contrast with the Lyot stop of a lower efficiency rather than higher throughput because the planet/disk detection is often contrast limited (see also § 9).

It is also noted that the pixel scale is over-sampled by a factor of two or more at the H and

K bands. Therefore, we can make a "binning" of 2x2 or 3x3 in the software. This will reduce the noise ($15e^-$) by a factor 2 or 3, or $8e^-$ or $5e^-$ equivalent. On the other hand, as described in § 3.2.3, the readout noise can also be reduced with the Fowler sampling. Therefore, the values of the limiting magnitudes depend on the observing modes and methods.

Since HiCIAO has several imaging modes to enhance contrast, we will describe test observations of each mode (see Fig. 3.6) in detail in the sections below. We also include a discussion of the new angular differential imaging (ADI) mode, which has produced impressive contrasts in the literature. ADI was not in the original HiCIAO CDR document, but it was easily implemented in HiCIAO because it requires no hardware changes.

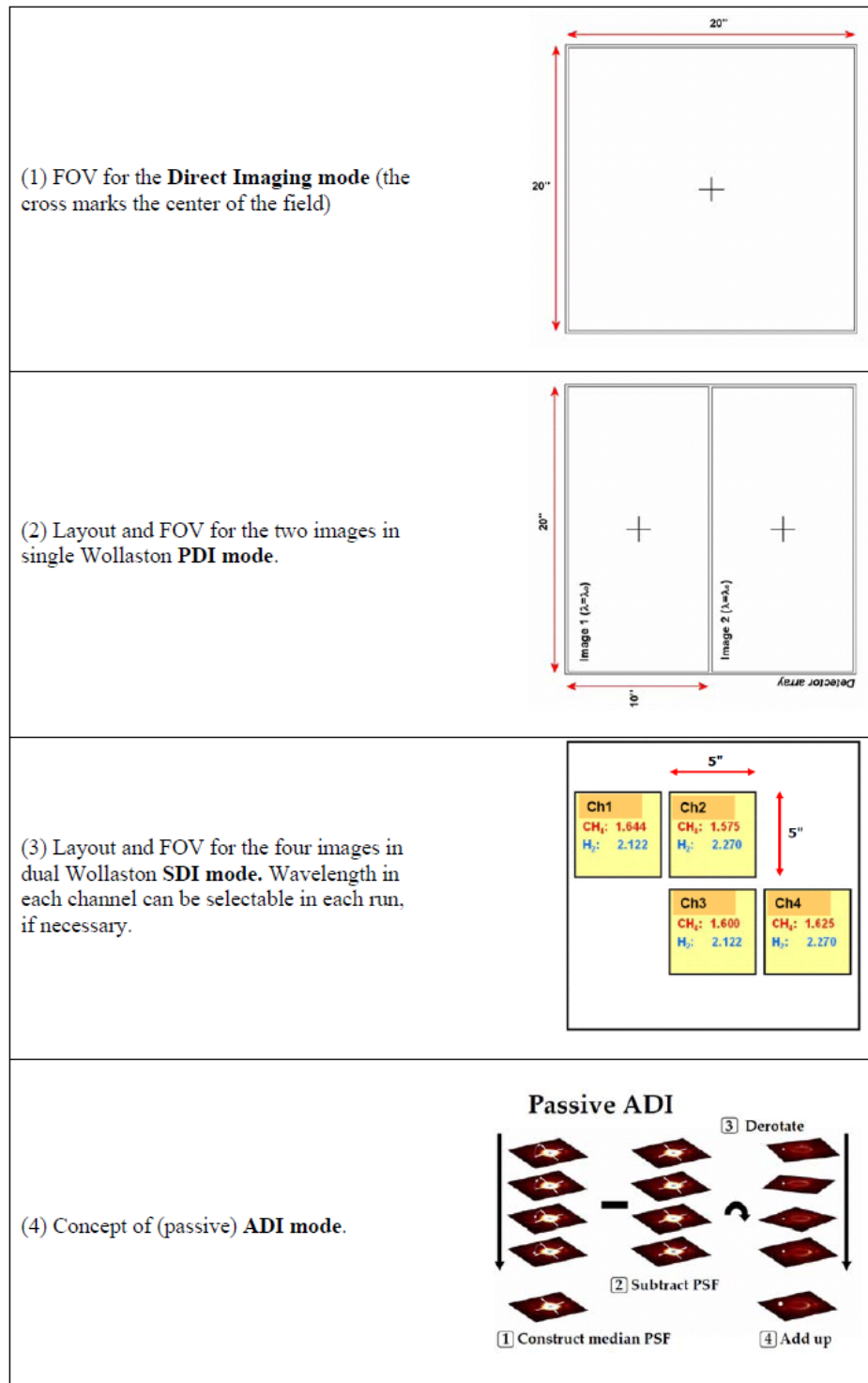


Figure 3.6: Observing modes of HiCIAO (DI, PDI, SDI, ADI).

4. Direct Imaging (DI) mode performance

4.1 Observations

In order to evaluate the performance with the direct imaging (DI) mode, we carried out imaging observations in the H and Ks bands on 2009 May 01. We used the coronagraph, a combination of a circular occulting mask at the first focal plane and a Lyot stop with spider patterns at the pupil plane. The coronagraphic mask has a transmission of $\sim 0.01\%$. We used 2 kinds of occulting masks with the diameters of $0.''3$ and $0.''6$. The target is a bright star; GJ564 (HD130948). This target has a binary brown dwarf pair at $2.''6$ (Potter et al. 2002). However it appears unresolved due to an orbital motion (Dupuy et al. 2009). The AO guide star is the central star itself, since our target stars are enough bright in R band where AO monitors atmospheric turbulence. Using the AO under the natural seeing (H band) of $\sim 0.''5$, the spatial resolutions (FWHMs) were improved to be as good as $0.''06$ and $0.''07$ in the H and Ks bands, respectively. As a photometric standard star, we used the object itself and performed a photometric calibration using the 2MASS Point Source Catalog. The other parameters of GJ564 show the Table 4.1 below.

Table 4.1 Observed target

Object	RA(2000)	Dec(2000)	SpT	D(pc)	Age(My)	R	H	Ks	Ref
GJ564 (HD130948)	$14^{\text{h}}50^{\text{m}}15.81^{\text{s}}$	$+23^{\text{d}}54^{\text{m}}42.5^{\text{s}}$	G2V	17.9	≤ 1000	5.5	4.7	4.5	Potter02

Typical observing procedures are as follows:

1. Acquire target
2. Check field and set AO point
3. Lyot stop adjustment
 - a. Take image before adjustment (strong spider pattern)
 - b. Check with pupil viewer
 - c. Adjust Lyot stop, if necessary
 - d. Take image after adjustment
4. Tune AO parameters
5. Insert near-IR neutral-density (ND) filter
6. Check unsaturated AO PSF with ND filter
7. Remove ND filter
8. Insert occulting mask
9. Make mask centering
10. Take science exposures with occulted target

4.2 Data reduction

For de-stripping and dark-subtraction, see § 3.3.

4.2.1 Flat fielding

We compared dome-flats and twilight flats in the DI mode. Dome-flat frames of H and Ks bands were taken at the start of the night (01 May) and twilight-flat frames are taken at the end of the same night. We judge two flats are very similar with each other (0.6% in the whole array and 0.3% in the central 100×100 pixels). Either way will produce the same results. Therefore, in the DI data reduction, we used the twilight-flat with median filtering.

The upper-right corner has a very low quantum efficiency (QE) region as seen in Figure 4.1. Please note that this part is not used in the SDI mode and is not a problem for coronagraph observations even in the DI and PDI modes because the mask is usually used near the field center where the array is most uniform and has a highest QE.

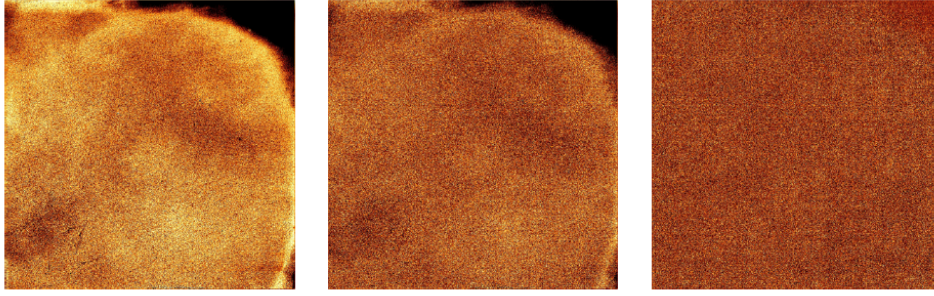


Figure 4.1: K band median flat frames. (*left*) Dome-flat, (*center*) Twilight-flat, (*right*) Dome/Twilight image.

4.3 AO performance with HiCIAO

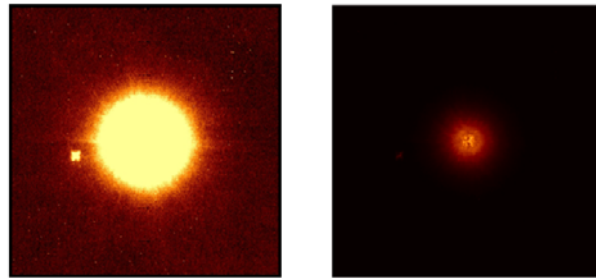
Performance of AO is characterized by a Strehl ratio and FWHM of the PSF. These parameters depend on the AO guide star magnitude, seeing, sky background and angular separation between the target and guide star. In general, performance of the AO system is better with a brighter guide star, at a better seeing, at smaller separations between the target and guide star, and at longer wavelengths.

Strehl ratio is measured by taking images without the occulting mask. Using the AO under the natural seeing (H band) of $\sim 0.5''$, the spatial resolution (FWHM) was improved to be as good as $0.06''$ and $0.07''$ in the H and K bands, respectively. These tests used the target as the AO reference star. The R band magnitude is 4.7. For comparison of observed PSFs, we made an ideal artificial PSF without any turbulence. Both peak intensities were normalized by that of PSF. As a result, we conclude the Strehl ratio is 0.38 and 0.67 in H and K bands, respectively. The AO188/HiCIAO Strehl ratio is about a factor of 2 higher than when using AO36/CIAO.

4.4 Contrast with self-subtraction

Self-subtraction of the measured image by its 180° rotated image can be a convenient high-contrast method for companion detection (but apparently not suitable for extended emission detection).

Raw and self-subtracted images of the H band coronagraph data using $0.3''$ mask are shown in Figures 4.2 and 4.3.



Figures 4.2: H band coronagraphic image using $0.3''$ mask + AO. The central star is located at the center of the image but is blocked by the mask. (*left*) $10.0'' \times 10.0''$ field-of-view. (*right*) the same but in different display range.

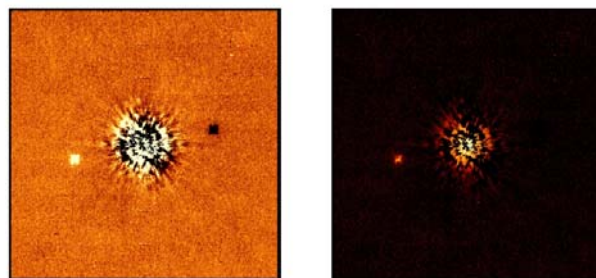


Figure 4.3: H band coronagraphic image using 0.3" mask + AO. Self-subtracted by 180° rotated image. The central star is located at the center of the image but is blocked by the mask. (*left*) 10.0"x10.0" field-of-view. (*right*) the same but in different display range.

The resultant radial contrast curve is shown in Figure 4.4.

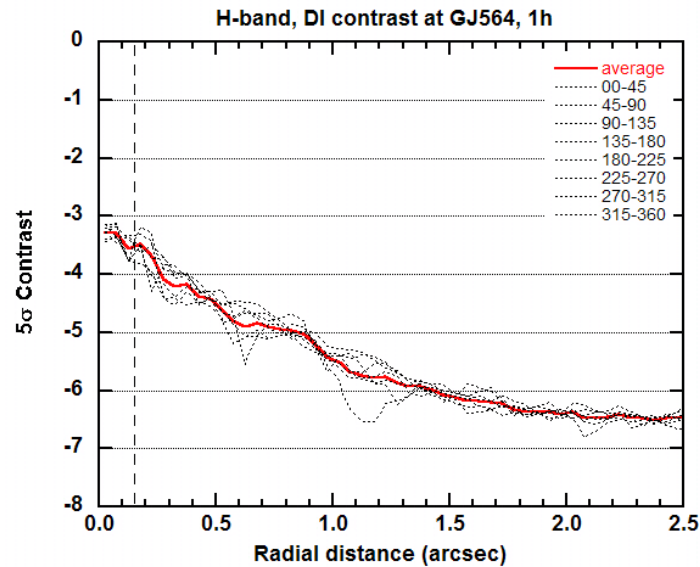


Figure 4.4: H band radial PSF 5σ profile normalized relative to the peak intensity, excluding a companion star. Dotted line shows the averaged profile of 8 directions in the angular section of 45° apex. Dotted lines show each profile converted to 1h integration time for 8 directions (45° each). Average profile is shown in red.

A similar experiment was made also at K band. The contrast profile is shown in Figure 4.5.

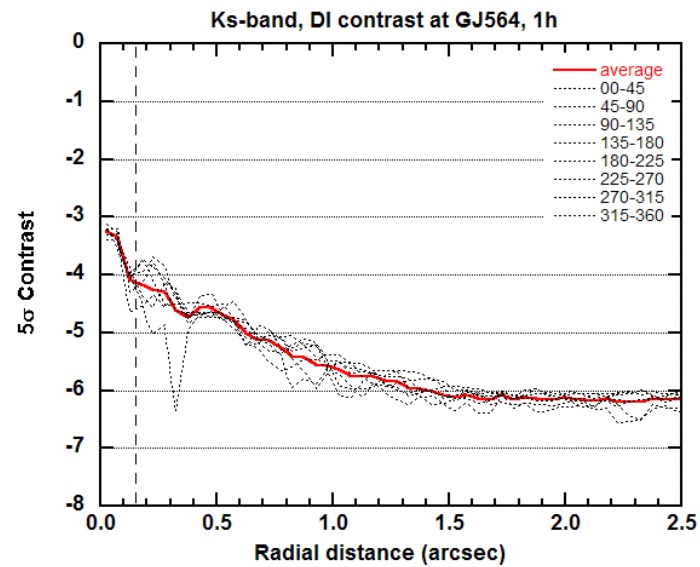


Figure 4.5: The same as Figure 4.4 but K band.

We also checked the contrast with a larger mask (0.6") with the same star and found no significant difference is seen in the achieved contrast. In contrast, the K band contrast is slightly better.

4.5 DI mode summary

In order to evaluate the performance in the DI mode, we conducted H and K band coronagraphic observations with AO188.

- The target is a bright star; GJ564 (R=5.5, H=4.7, and K=4.5).
- Using the AO, the spatial resolutions (FWHMs) of 0."06 and 0."07 were achieved in the H and K band, respectively.
- The Strehl ratios are 0.38 and 0.67 in the H and K bands, respectively.
- A contrast after the self-PSF subtraction is good at a large angle ($r > 1."$ 0); $\sim 10^{-5.5}$ at 1.0".
- The contrast is more or less the same for 0.6" mask and slightly better for the K band.
- Compared with the previous instrument (CIAO+AO36), the contrast of HiCIAO+AO188 was about 10 times better than before in the DI mode.
- The DI mode will be a SEEDS observing mode of choice if one needs a larger field of view (20"x20") but its contrast might not be as good as other modes near the central star. So, this mode is useful for far-companion check with a short integration time for each object of interest.

5. Spectral Differential Imaging (SDI) mode performance

The SDI mode is capable of taking four different polarization images (FOV=5"x5") simultaneously by using a double Wollaston prism installed in the warm fore-optics module of HiCIAO. These images are detected on the single HAWAII-2 detector (2Kx2K elements) after passing through narrow band filters located inside the cold camera module of HiCIAO. The subtraction of different wavelength images taken at the same time, i.e., spectral differential imaging, enables significant suppression of speckles produced by the bright primary star, providing better inner working angle for the search of planetary companions with specific spectral features (e.g., methane absorption at 1.6 micron).

5.1 Observations

Engineering observations for the SDI-mode were conducted on 2009 May 2 and Aug 5. The narrow band filters employed for the observations were the methane band filters covering two wavelengths tracing continuum (methane/off), 1.575 and 1.600 micron for the channel 2 and 3, and two wavelengths with absorption (methane/on), 1.644 and 1.625 micron for the channels 1 and 4.

The targets observed for the contrast performance evaluation in the SDI-mode are HIP 59532 (May 2: H=5.9 mag, G5V), HIP 104214 (Aug 5: H=2.5 mag, K5V), and HR 8799 (Aug 5: H=5.3 mag, A5V). The effective exposure times for each target are 2250 s (150 s x 15 frames), 500 s (10 s x 50 frames), and 800 s (100 s x 8 frames) for HIP 59532, HIP 104214, and HR 8799, respectively.

The observation procedures for the SDI-mode are as follows. First, the telescope was pointed toward the target by taking exposures in the DI mode to search the target. Second, adaptive optics (AO188) was turned on, and the star was moved to the center of the frame. Third, the observing mode was changed to the pupil-viewing mode in order to register the position of Lyot-stop with telescope spider and mirror structure. After the registration of Lyot-stop, observing mode was changed to the SDI mode with methane filters, and then short exposures were taken without the coronagraphic mask. This is for measuring the shape of the stellar PSF on the SDI images. The star was then moved to the coronagraphic mask position for long exposures. The coronagraphic mask with 0.3" diameter was used, because the atmospheric condition was enough stable and good in seeing. The mask center and the center of star were carefully registered using the shift aided by the AO tip/tilt. Finally, long exposures were taken. The slight (sub-pixel) misalignment between the mask and star center due to the telescope/AO tracking was corrected at each exposure.

For calibration, we obtained dome flat frames in the SDI mode before the observations. In order to correct the distortion of each channel image, we obtained calibration frames by locating an illumination source and a pinhole grid in front of the HiCIAO fore-optics module.

5.2 Data reduction

First, detector systematics on the raw images are corrected based on the method similar to the DI mode (de-stripping). For flat fielding, a normalized dome flat image obtained in the SDI mode was used. Bad pixels on the detector were searched/detected by using a Laplacian filtering technique, and subsequently interpolated using the values of neighboring pixels. Second, the region of 5" field-of-view around each SDI channel (Ch1-4) was extracted from the original image. Finally, the subtraction of one channel from another channel (SDI subtraction) was conducted after the correction of distortion and speckle patterns in each channel.

The final process is the most critical part in order to suppress the (speckle) residuals in SDI subtraction. Though SDI channel images are obtained simultaneously, (1) they suffer different distortion by the optical components in HiCIAO, and furthermore, (2) the speckle patterns around the primary star are different, because each SDI channel observes different wavelengths. In addition to these corrections, (3) centering of the primary star and the scaling in intensity are necessary before subtraction.

For the correction of (1), transformations based on precise pinhole grid images can be used for each channel, and for (2) a transformation function predicted by the HiCIAO optical design

can be used. The linear transformations including (1)- (3) were conducted before subtracting one channel from another in order to correct distortion and different speckle patterns. The best parameters in the linear transformations were determined by minimizing the sum of squared residuals for a number of SDI subtractions performed using various parameter values. Note that linear transformations of images are conducted through the calculations in the frequency space in order to preserve the resolution of original images.

5.3 Contrast

5.3.1 Method

For the evaluations of achievable contrast in the SDI mode, the radial relative intensity profiles were made following the same methods as used in DI and PDI modes. First, the intensity scale of the SDI subtraction image was converted into the relative value against the peak intensity of the stellar PSF measured using the short exposure SDI image without mask. Second, the SDI subtraction image was smoothed with 5 pixels, λ/D at H band. In order to evaluate the position angle dependence in the contrast performance, the image was divided into eight fan-shaped areas with 45° separation, and then annuli with 5 pixel width/spacing were set toward each octant. In each octant, the pixel-to-pixel standard deviation (5σ) was measured in the arc regions enclosed by the fan and each annulus. We obtained eight radial profiles of 5σ values relative to the peak intensity in this way. We also obtained averaged profile by taking the mean of 5σ values measured at the same radial distances. Finally, we converted the relative 5σ values into the ones equivalent to the 1-hour effective exposures by assuming that the noise behavior follows $1/\sqrt{t}$ relationship (as in the simulation in the CDR document).

5.3.2 Result

We demonstrate a SDI subtraction image and its contrast curve in Fig.5.1 and Fig.5.2. The subtraction results of HIP 104214 between Ch3 and Ch2 combined for 50 frames are shown. Note that we have tested all the combinations in the SDI channel pairs, and confirmed the differences in SDI subtraction performance were within the factor of 2.

The obtained (1-hour equivalent) contrast values are 1.1×10^{-4} (at $r=0.15''$), 5.5×10^{-5} ($0.30''$), 2.2×10^{-5} ($0.50''$), 4.7×10^{-6} ($1.00''$), and 3.8×10^{-6} ($1.20''$). [or -3.94 (at $r=0.15''$), -4.26 ($0.30''$), -4.65 ($0.50''$), -5.32 ($1.00''$), and -5.42 ($1.20''$)] These values are consistent with the simulation result of 1-hour performance in the CDR document. In particular, the SDI mode can achieve the highest contrast to CH₄-bearing objects at inner regions. The contrast values in the region beyond the radial distance greater than $\sim 1.2''$ are considered to be read-out noise limited. Contrast curves obtained for the other fainter targets, HIP 59532 and HR 8799, are consistent with HIP 104214, although their contrast curve became readout noise limited at smaller radius, $r \sim 0.8''$.

5.3.3 Supplement 1: Noise behavior as a function of radius

As described above, we derived the contrast curve of HIP 104214 equivalent for the 1-hour effective exposure time based on the less integrated SDI dataset (500 s or 50 frames x 10 s). The employed assumption that the noise reduction rate follows $1/\sqrt{t}$ law is appropriate when we compare the observed performance with our simulated 1-hour performance derived using the same assumption. However, in reality, the $1/\sqrt{t}$ noise reduction should not be applied especially in the speckle dominated region close to the bright central star.

We evaluated the behavior of noise reduction as a function of radius by comparing the standard deviation of single exposure frame with the combined frame of multiple exposures. Fig 5.3 shows the radial profile of the ratio of standard deviation between single ($N=1$) and combined ($N=50$) SDI frames of HIP 104214. The blue and black solid lines show the measurements and its polynomial fit.

It is clearly shown that the solid line approaches the lower broken line, $\sim 0.14 = 1/\sqrt{50}$, toward larger radius, indicating that the noise effectively decreases with increasing exposure time following the $1/\sqrt{t}$ law at least at $r > 1.5''$. The noise reduction rate gets degraded toward the inner region due to the effect that the speckle noise is not perfectly suppressed.

Though the deviations from the $1/\sqrt{t}$ law appear in the inner region, the solid line is still below the upper broken line ($=1$) even at the radius of occulting mask edge ($r=0.15''$); the speckle noise is partially subtracted even at the innermost region, so that the improvement of standard deviation is achieved in all the radius of the combined image.

On the basis of the empirically obtained noise reduction relationship, more realistic estimation of the 1-hour contrast curve was conducted. In Fig 5.2, the blue solid line shows the 1-hour equivalent performance scaled from the 500 s exposure data by considering the empirical correction of the degradation from $1/\sqrt{t}$ law. The deviation in the contrast performance with and without the correction is small; The blue solid line deviates from the contrast curve without the correction by a factor of ~ 2 at most in the vicinity of mask edge, and beyond the $r=0.5''$ these two curves become identical within error bars. We thus believe that the 1-hour contrast performance consistent with our simulated value can be obtained in the SDI-mode observations of the SEEDS science run.

5.3.4 Supplement 2: Detectability of companion without methane feature

It is noteworthy that the SDI technique relies on the methane feature in a planet spectrum. The companions without methane absorption can escape from detection since they will be subtracted out with the host star PSF. Therefore, the use of the word sensitivity should be qualified by the methane properties of planets. This argument is true for the companions with small separation angle, but not in the case for the large separation companions.

In the SDI subtraction procedure, one channel image is subtracted by the another channel image enlarged by the factor of their wavelength ratio in order to match the size of speckle pattern around the central star. The position of a companion in each channel can thus be displaced to make a pair of negative and positive peaks in the SDI subtracted image. Since the degree of displacement increases with increasing separation from the central star, the PSF of large separation companions cannot be canceled out in the SDI subtraction image even if the companions do not have methane feature.

Fig 5.4 shows the simple simulation of how methane-free companion's PSF is canceled after the SDI subtraction. In the case of the subtraction between ch1 (1.644 micron) and ch4 (1.575 micron), the companion's PSF peak becomes only 15% of the original value at $r=0.15''$ after the subtraction, but the percentage rapidly increases toward the larger radius, e.g., 50% at $r=0.6''$ and 80% at $r=1.0''$, enabling the detection of companions even without methane feature.

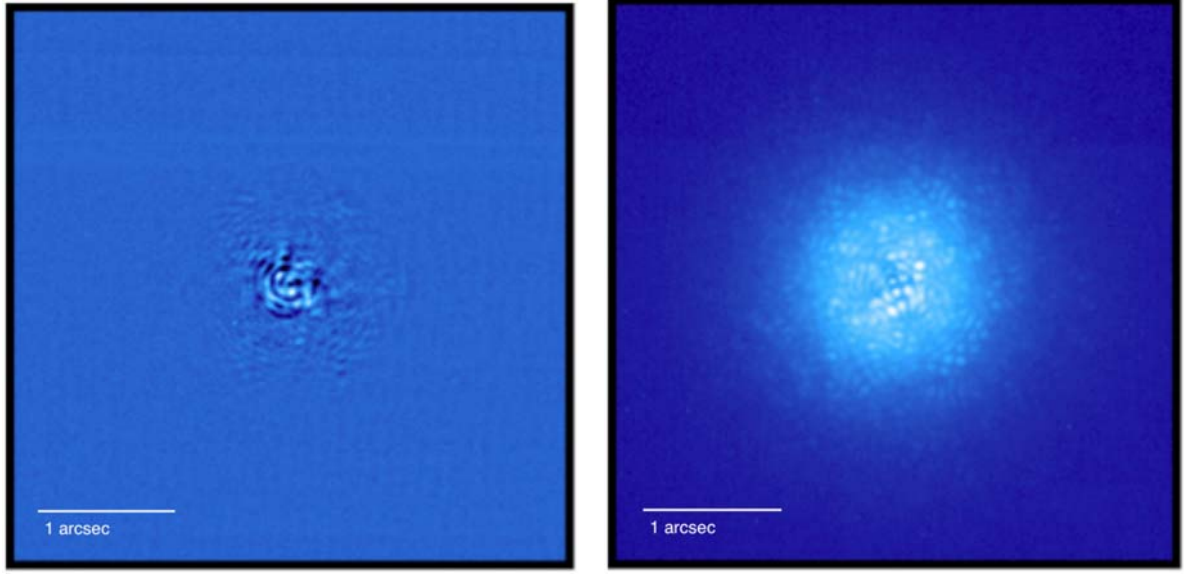


Figure 5.1: (*Left*): SDI subtraction (Ch3 - Ch2) image of HIP 104214. 50 frames with 10 s exposure were combined after the subtraction. The size of the image is 4". The color of the image is in logarithmic scale. (*Right*): The SDI image before the subtraction (Ch2).

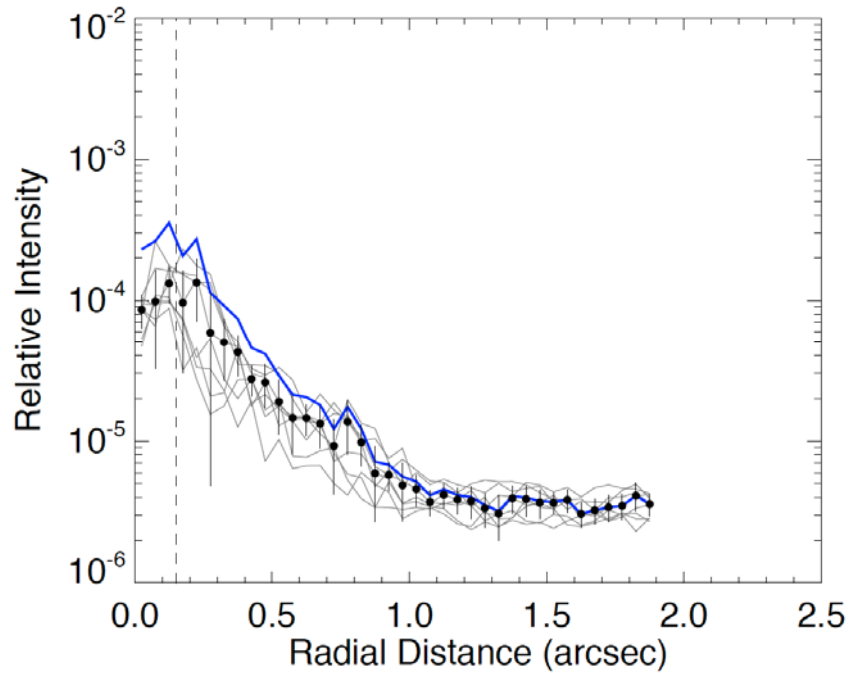


Figure 5.2: Relative intensity (5-sigma) profile of SDI subtraction image (Ch3 - Ch2). Black filled circles with error bars denote averaged 5-sigma value in each octant for the 1-hour effective exposure time. Gray lines show the contrast curves for each octant. The vertical broken line shows the radius of the occulting mask ($r=0.15''$). The blue solid line shows the same data as black filled circles, but the empirically estimated degradation from $1/\sqrt{t}$ noise reduction law in each radius is taken into account (see, section 5.3.3).

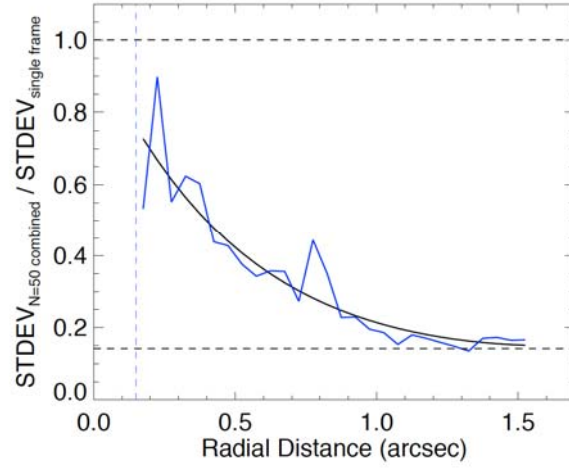


Fig 5.3: Radial profile of the ratio of standard deviation between single ($N=1$) and combined ($N=50$) SDI frames. The blue and black solid lines show the measurements and its polynomial fit. The lower horizontal broken line shows the level of $1/\sqrt{50}$, corresponding to the $1/\sqrt{t}$ noise behavior. The vertical broken line shows the radius of occulting mask ($r=0.15''$).

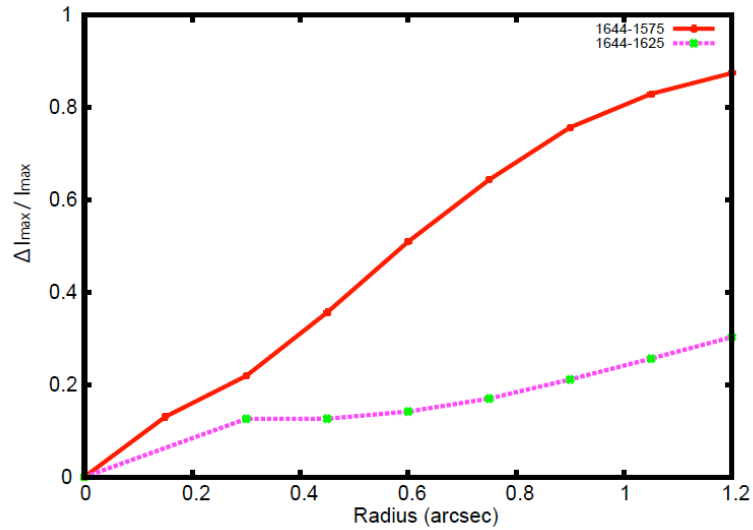


Fig 5.4: This diagram shows how the PSF of companion without methane feature is canceled in the SDI subtraction process. The horizontal axis shows the position of the companion, and the vertical axis shows the ratio of companion's PSF peak before and after the SDI subtraction. The results for the two channel pairs are shown; one is the case of the largest wavelength difference (red line, Ch1: 1.644 micron and Ch2: 1.575 micron), and another is the smallest (dotted line, Ch3: 1.600 micron and Ch4: 1.625 micron).

6. Angular Differential Imaging (ADI) mode performance

Since the ADI technique does not require any specialized optics, it can be combined with any of the other observation modes of HiCIAO (DI, SDI, PDI). For simplicity, we chose the DI configuration (20"x20") for the commissioning of HiCIAO's ADI capability. The instrument setup is identical to the one used for conventional DI observations; the only difference lies in the operation of the image rotator (IMR). The rotation angle is controlled such as to keep the orientation of the *pupil* (rather than the field) constant on the detector. As a result, the target star's PSF – including the speckle distribution and the residual spider pattern – remains fixed on the detector throughout the observation, while any planet in the field of view moves along an arc as the sky rotates. During data reduction, this sequence of images can be exploited to estimate and subtract the fixed stellar PSF while leaving the planet signals intact. Finally, the frames are de-rotated into a fixed position angle and co-added. We note that the ADI technique works equally well on companions with any spectral type and specifically, it is not dependent on any CH₄ or H₂ spectral features.

6.1 Observations

Engineering observations for the ADI mode were conducted on May 2 and May 11, 2009. Three targets were observed:

- GJ 564 = HD 130948. This target was chosen to gauge the high-contrast performance of HiCIAO's ADI mode. It offers good AO performance ($R = 5.5$), a high rate of field rotation, and a known binary pair of brown dwarfs at a separation of 2.6". It was observed with the 0.6" coronagraph for a net exposure time of 6 minutes in H band and for 13 minutes in K band.
- 1RXS J160929.1-210524 (abbreviated as 1RXS1609). This target explores the regime of marginal AO performance ($R = 11.8$) and features a known 8 M_J planet candidate at a separation of 2.2" (Lafrenière et al. 2008). Net exposure time was 6 minutes in H band, without coronagraph.

The observation procedure was the same as for regular DI observations, starting with slewing and target acquisition, closing of the AO loop and parameter tuning, alignment of the Lyot stop in pupil-viewing mode, and centering of the Lyot coronagraphic mask. After this target set-up, the ADI exposures were taken. The targets were observed as close to their meridian transit as possible to maximize the field rotation and AO performance.

The data was dark-subtracted and divided by a flat field. The field distortion was corrected using a map that was produced by five dithered images of the crowded core of the M5 open cluster were taken. Comparison of the known pointing offsets and the observed shifts of the star positions yielded the fit parameters for the distortion model.

6.2 Data reduction

The data were reduced using a custom set of IDL routines that implement the "LOCI" algorithm (Locally Optimized Combination of Images, Lafrenière et al. 2007). David Lafrenière generously provided a functional LOCI pipeline for Gemini Observatory data to the HiCIAO team. This pipeline was adapted to the HiCIAO instrument by the ADI team.

After the usual dark subtraction, flat-fielding and distortion corrections, the frames were carefully registered to their center. As a very conservative form of high-pass spatial filtering, a radial profile was subtracted from each frame. The LOCI code then divided each frame into annuli and segments, and for each segment a localized background was subtracted. Each segment background is computed from all other frames in the sequence by applying an optimization process that minimizes the image residuals. Finally, the resulting frames were derotated to position angle zero and co-added to produce the high-contrast output image.

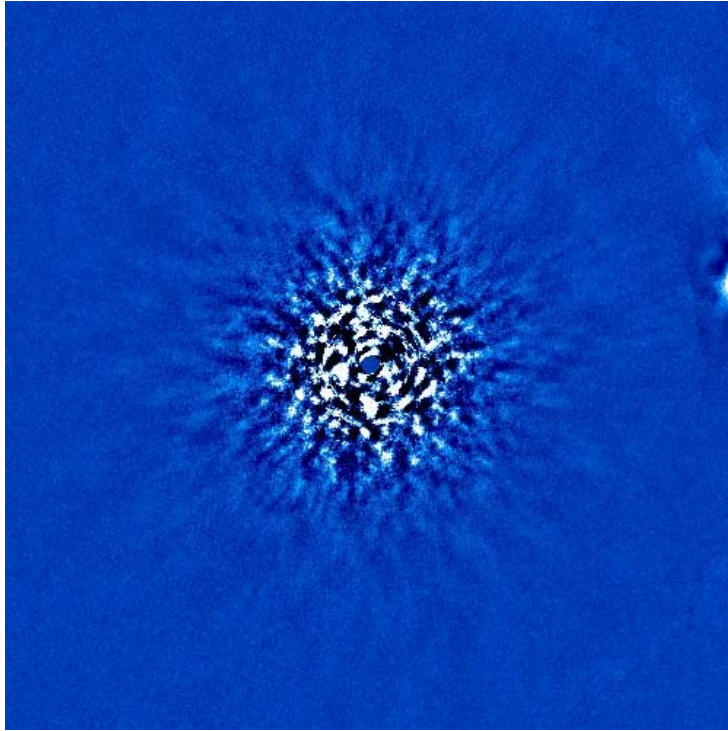
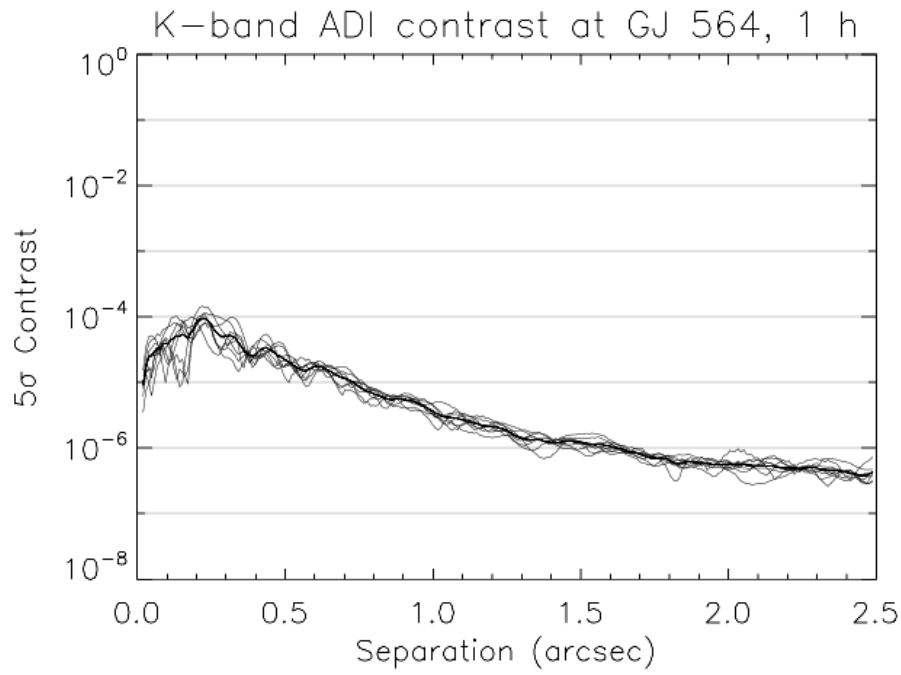
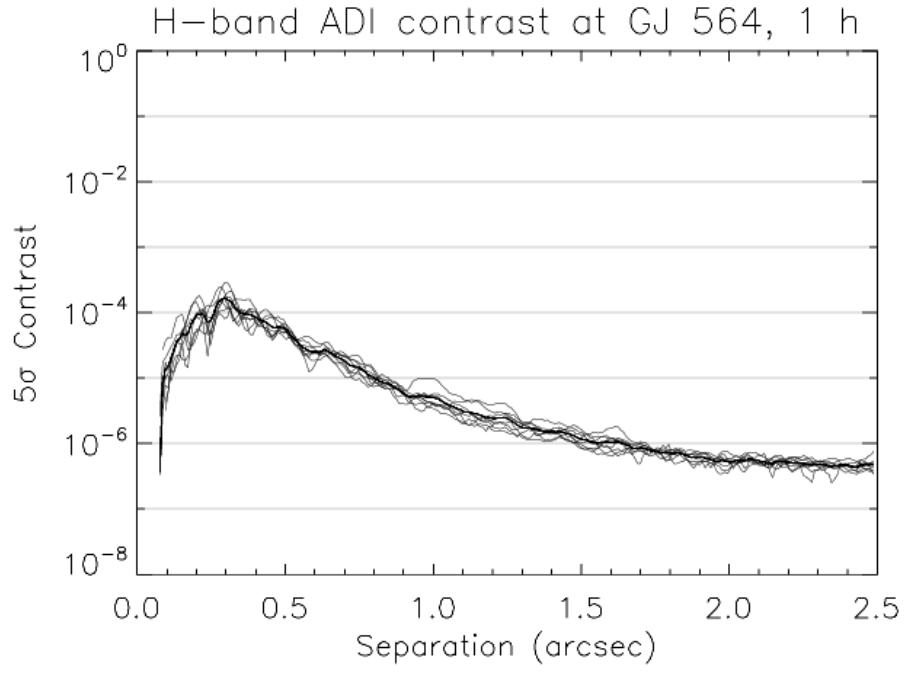


Figure 6.1: Center of the final image from K band ADI observations of GJ 564. The binary brown dwarf is visible on the right-hand edge.

6.3 Contrast

For the sake of consistency, we employ the same recipe for the calculation of the contrast curves as used for the other observing modes. The output image was convolved (smoothed) with a 5x5 pixel flat circular aperture, which corresponds to the "footprint" of a PSF core, and normalized by the flux of the target star. We then split the image into 45° octants and calculated the pixel-wise standard deviation in each octant as a function of separation from the center. Note that due to the convolution, this value described the variability of the image on the spatial scale of a planet's PSF core. We multiplied this curve by a factor of 5 to obtain the 5σ detection level. Furthermore, the curve is divided by the "partial subtraction factor", a separation-dependent parameter between 0 and 1 describing the percentage of planet flux that survives the LOCI subtraction, which is calculated by inserting 'test' companions into the raw data and processing it through the LOCI pipeline. Finally, the curve is scaled up to an integration time of 1 hour, assuming that the noise level decreases with $1/\sqrt{t}$.

Figure 1 shows a fully reduced and LOCI-subtracted K band image of the young star GJ 564. The contrast performance curves for the GJ 564 H and K band images are presented in Figure 2 and 3. Figure 4 shows our clear detection of the 8 M_J planet of 1RXS1609 in H band. We can even detect such planetary-mass companions down to $r=0.3''$ in this image.



(above) Figure 6.2: H band ADI contrast curve derived from GJ 564. The edge of the coronagraphic mask is at 0.3".

(below) Figure 6.3: K band ADI contrast curve derived from GJ 564. The edge of the coronagraphic mask is at 0.3".

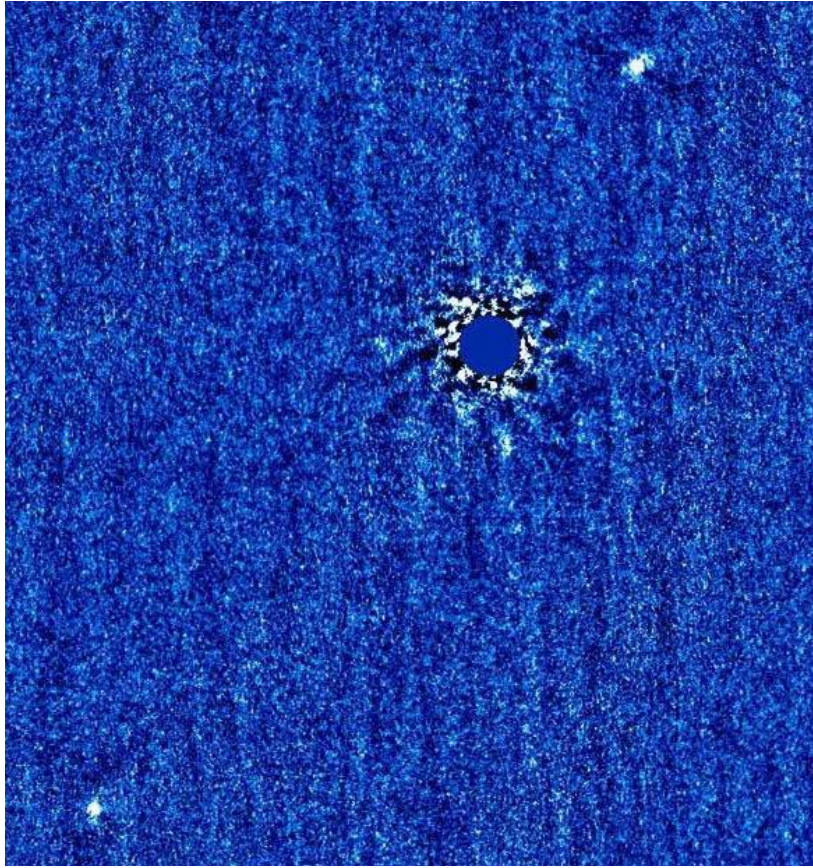


Figure 6.4: Center of the final image from H band ADI observations of 1RXS1609. The bright spot on the upper right is the 8 M_J planet discovered by Lafrenière et al. (2008). The similarly bright spot on the lower left is a background star.

6.4 ADI observations of HR 8799 during Subaru/HiCIAO commissioning

The three planets HR 8799 bcd were imaged by Marois et al. (2008) in the near infrared, orbiting the star in an approximately face-on configuration at separations of 1.73", 0.95", and 0.63", apparent H-band magnitudes of 17.8, 16.9, and 16.8, and H-band contrasts of $10^{-5.0}$, $10^{-4.6}$, and $10^{-4.6}$. For this reason, the star was selected to serve as a benchmark test to compare the performance of the different modes as directly as possible. The target was observed for an equal amount of time in three different modes: SDI, ADI, and DI. Here we report the results of the ADI observation.

A total of 27 frames composed of 2 co-adds of 9.75 seconds were taken over the course of 18 minutes on telescope, resulting in 8:45 min of net exposure time. The field rotated by 7.5° during that time, allowing for background subtraction with the LOCI algorithm down to separations of $\sim 0.4''$. Even in this short observation, all three planets are visible on the resulting image. The corresponding signal-to-noise map is shown in Figure 6.5. The planets HR 8799 bcd achieve S/N ratios of 7.1, 4.3, and 4.5. Although there are residual structures of comparable brightness to the inner two planets in the image, the planets can be clearly identified by their point-source-like shape. A longer ADI observation would provide more field rotation and thus more independent samples of the spurious background structure, allowing a significantly better subtraction and a cleaner detection of the planets.

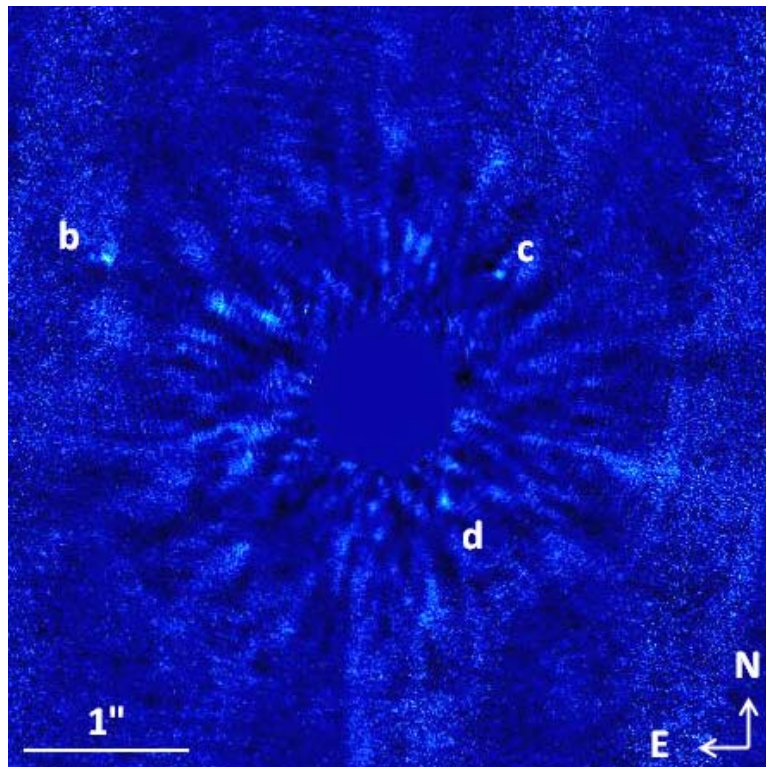


Figure 6.5: Center of the signal-to-noise map generated from H-band ADI observations (~ 9 min) of HR 8799. All three planets discovered by Marois et al. (2008) are detected. The horizontal white bar corresponds to $1''$.

Fig. 6.6 shows a direct imaging data with self-subtraction (180° rotated), in which only "bc" are ("b" is clearly, while "c" is "barely") detected. Therefore, the merit of the ADI over the simple DI mode is clear.

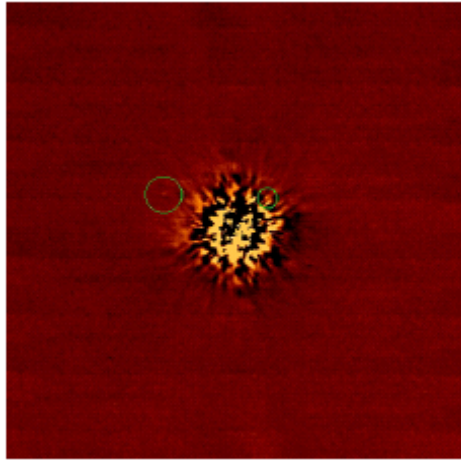


Figure 6.6: H-band DI observations (~15 min) of HR 8799. Only two planets discovered by Marois et al. (2008) are detected. The mask size is 0.3". The field-of-view is 10"x10".

7. Polarization Differential Imaging (PDI) mode performance

We employ a polarizing (single) Wollaston beam splitter in the PDI mode. Wollaston prism divides incident light in two and produces the same two images on the same detector, thus minimizing the non-common path errors.

If the central star is not polarized, the speckles surround the star are also not polarized, and thus, the split lights have equal brightness, therefore we can suppress the speckle noise by subtracting the two images with each other.

If the objects around central star are polarized such as circumstellar disks or envelopes, the separated light has unequal brightness, and thus, we can detect the polarized objects with a small inner working angle by subtracting the two images (i.e., dual beam polarimetry).

Since the PDI mode has a field-of-view of 1000×2000 pixels ($10'' \times 20''$) which is wider than that of SDI mode (500×500 pixels), we could also use this mode as a wide-field SDI mode with the spectral differential filter in order to search the wide-separated companions.

7.1 Observations

H band PDI observations have been conducted on 2009 May 11 and August 3. Since adaptive optics were employed in these observations, the good and stable seeing enabled us to achieve a high spatial resolution (FWHM) of $0.070''$ in the H band. During the observations for HIP 98549 which is a nearby non-polarized star of $H = 4.9$ mag, the half waveplate was not rotated in order to measure the contrast. We took 2 frames of $9.7 \text{ s} \times 1$ co-adds integration without a occulting mask in order to measure the PSF, and 12 frames of $25 \text{ s} \times 1$ co-adds integration with a occulting mask of $0.3''$.

For the observations of HIP 74419 which is also a nearby non-polarized star of $H = 10.4$ mag, the polarizations were measured by rotating the half waveplate at four angular positions (0° , 22.5° , 45° , and 67.5°) in order to measure the non-polarization. We observed 14 sets for the object and 13 s integration per waveplate position without mask.

7.2 Data reduction

The data were reduced in the standard manner of infrared image reductions: subtracting a dark-frame and dividing by a flat-frame. Then we corrected the distortion between the two split images by using the pinhole image taken in the same day, which leads the positional accuracy of the split two images to be within ~ 0.1 pixels. We also used the IRAF packages of GEOMAP and GEOTRAN for this correction. Note that since M5 data were employed to correct the distortion for images of HIP 74419, the positional accuracy of the split two images are within ~ 0.2 pixels.

To correct the instrumental effect on the linear polarization, we apply the linear relation between the observed intensity ratio and the Stokes parameter of objects as

$$r \equiv \frac{|E_x|^2 - |E_y|^2}{|E_x|^2 + |E_y|^2} = c_0 + c_1 Q + c_2 U$$

where E_x and E_y are horizontal and vertical electric field on the detector, and the coefficients depend on the angles of tertiary mirror / image rotator / retarder and the observed wavelength. We solve the Stokes Q and U parameters from a pair of this equation of different retarder angles, and have the amplitude and angle of linear polarization of object.

7.3 Contrast in "Intensity"

We estimated the contrast in the PDI mode by the same manner of the DI and SDI modes: converting the PSF peak without the mask into the subtracted object with the mask and smoothing the subtracted images with 5 pixels. Then, the same as with the DI and SDI modes, we estimated the position angle dependence of the contrast by dividing the subtracted object into eight parts with 45° separation. We derived the pixel-to-pixel standard deviation with 5 pixel annuli in the each part, and then, regarded 5σ relative to the PSF peak as the contrast.

Finally, the derived contrast for 300 s exposures were converted into the 1-hour effective exposures by assuming that the noise behavior follows $1/\sqrt{t}$ relationship.

Fig. 7.1 shows the derived contrast curve by the above procedures. The obtained contrast values are 9.8×10^{-5} (at $r=0.175''$), 2.4×10^{-5} ($0.325''$), 1.4×10^{-5} ($0.525''$). The contrast values in the region beyond the radial distance greater than $\sim 2.0''$ are considered to be read-out noise limited in this test.

7.4 Unpolarized stars

We also estimate how close to the central-star is unpolarized. In the same manner as the case of the contrast curve, the position angle dependence of the Stokes Q and U have been estimated. We derived the averaged Stokes Q and U with 5 pixels annuli in each fan shape, and then, instrumental polarization involved in derived the Stokes Q and U are corrected by the model parameter. Finally, we calculated the degrees of polarization P.

Fig.7.2 shows the images and the curve of degrees of polarization P. In Fig. 7.2(a1) and (a2), the Stokes Q and U are derived from the left and right images at two angular positions, e.g., 0° and 22.5° . On the other hand, in Fig. 7.2(b1) and (b2), those are derived from only the left image at four angular positions, i.e., 0° , 22.5° , 45° , and 67.5° . The obtained P values in Fig.7.2(a2) are roughly 4% within $r=0.4''$. On the other hand, those in Fig. 7.2(b2) are roughly larger than 4% within $r=0.4''$. When the circumstellar disk has larger than $\sim 5\%$ level polarization, dual-beam polarimetry allows us to investigate the inner regions even within $r=0.4''$ down to $<0.1''$.

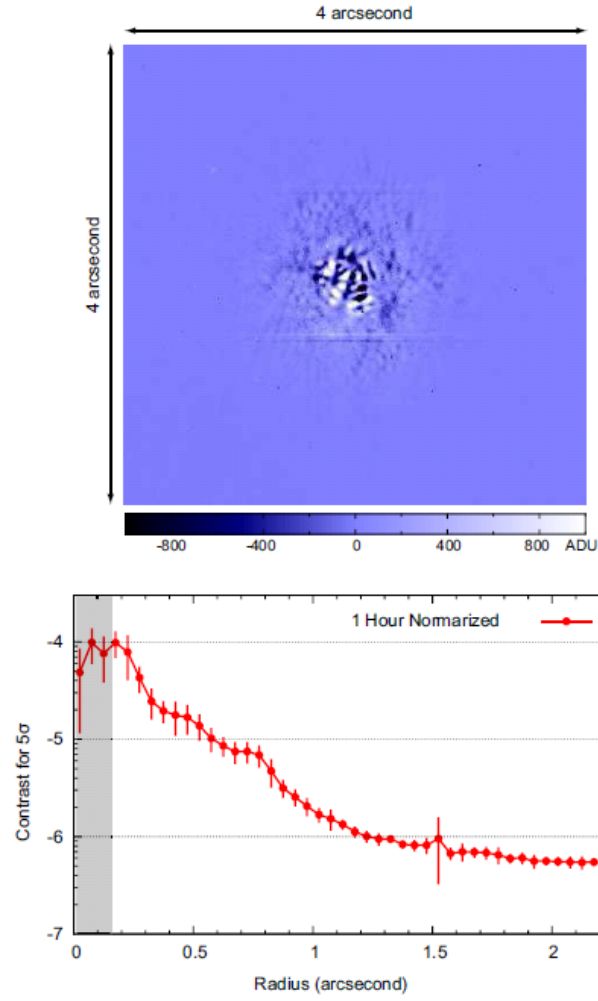


Fig. 7.1: The "Intensity" contrast measurement for HIP 98549 which is a nearby non-polarized star of $H = 4.9$ mag. The hatched part within $0.15''$ represents the region within a occulting mask of $0.3''$.

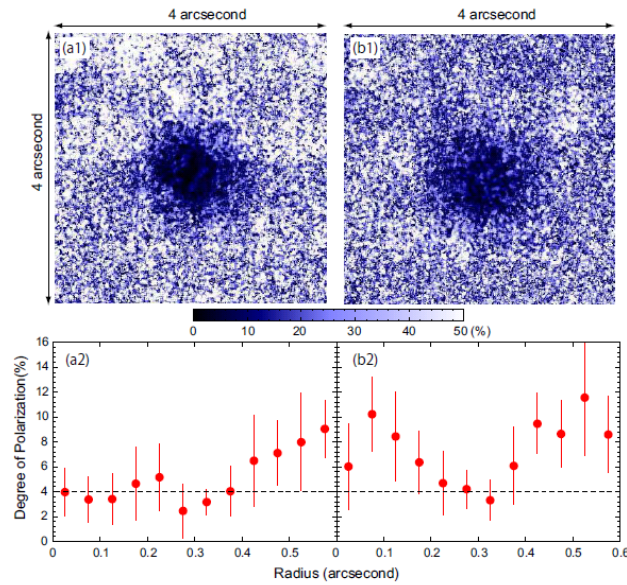


Fig. 7.2: The non-polarization for HIP 74419 which is a nearby non-polarized star of $H = 10.4$ mag. Left figures (a1 and 2); polarization is derived from two angular positions, e.g., 0° and 22.5° . Right figures (b1 and 2); polarization is derived from four angular positions, i.e., 0° , 22.5° , 45° and 67.5° .

8 . Aperture polarization performance and extended object

8.1 Unpolarized stars

We observed unpolarized star (candidate) HIP74419 (G2) with the PDI mode at the waveplate PA of 0°, 22.5°, 45°, and 67.5° on 2009 May 11. The waveplate was tracked both telescope image rotation and elevation change. The images are dithered by 100 pix. The waveband was H, and the exposure time was 13 s.

In order to evaluate the polarization levels,

$$r = (I_{\text{horiz}} - I_{\text{vert}}) / (I_{\text{horiz}} + I_{\text{vert}})$$

was calculated for 14 combinations of the waveplate angles where I_{horiz} and I_{vert} are signals at left and right image.

Polarization was derived as follows:

$$\begin{pmatrix} E_{\text{horiz}} \\ E_{\text{vert}} \end{pmatrix} = FX \begin{pmatrix} E_d \\ E_n \end{pmatrix}$$

where $E(E_{\text{horiz}}, E_{\text{vert}})$ is the E vector on the PDI mode was connected to the $E(E_d, E_n)$, the E vector on the sky. We will use F and X as follows:

F: flat correction from dome flat data (May 11 and Feb 7 data)

X: Reflection at 3 AO mirrors with Ag coating and image rotation were modeled.

From these relations we derive Ps:

From (0, 22.5) data, $P = 0.6\%$ and $\theta = 64.8$ deg.

From (45, 67.5) data, $P = 0.9\%$ and $\theta = 74.2$ deg.

These are consistent within $\sim 1\%$.

Therefore, we conclude the polarization accuracy is at the $\sim 1\%$ level.

8.2 Polarization standard

We observed Elias19 as a linear polarized standard star with the PDI mode at J and H band on 2008 December 23. (We tried K band as well, but failed to take a frame within unsaturated level even without adaptive optics at this engineering phase). The half waveplate was tracked in sidereal mode, i.e. compensating the image rotation angle by alt-az telescope and elevation angle of the tertiary mirror to the Nasmyth platform, and was set offset angle of 0°, -22.5°, -45°, and -67.5°. The exposure time of each frame was 4.2 s and the total integration time was 80 s for J band, and 70 s for H band. A frame pair of offset angle of (0°, -22.5°) or (-45°, -67.5°) were processed to derive the polarization modulus and angle and the results are listed in the table below.

Elias 19 – linear polarization standard star

band	<P>	< σ_P >	< θ >	< σ_θ >	T[s]
J	3.4%	0.9%	22.1°	10.9°	80
H	2.6%	0.6%	40.4°	4.5°	70

With the standard deviations accounted, our results are comparable to the reliable measurements by Whittet et al. (1992) whose observations were done with a single element detector.

Elias 19 – Whittet et al. 1992

band	<P>	< θ >
J	3.06%	36°
H	1.94%	35°

The order of error of polarization intensity and angle are 1%, and 10° or less, respectively in this integration time. Elias 19 is bright in the near infrared region, and the measurements were done without the adaptive optics tuned so that the stellar PSFs were extend around 1.5 arcsec in radius. The photometric accuracy can be degraded due to this large PSF since the HiCIAO HgCdTe array output has position dependent residuals whose values are variable frame to frame. The nominal observation with the adaptive optics tuned should provide more precise results with longer exposure time.

8.3 Extended object

8.3.1 HL Tau

We observed HL Tau with HiCIAO PDI mode at J,H,K band on 2008 December 23 to see the performance of polarization measurement for extended objects. The total exposure times are 195, 195 and 479 s for J,H,K respectively. Observation procedure and data reductions for extended objects are parallel to those of stellar sources with the exception that spatial information is retained in reduction process to the final results. We corrected the geometrical distortion between the horizontal- and vertical-polarized ray subframes by expanding the horizontal one with factor 1.02 in column direction, and shift them in sub pixel order to mate the central peak positions of the paired sub-images. In this observation, we did not use the adaptive optics since HL Tau lacks a AO guide star in the observing field (so geometrical correction is not essential in this case).

The extension/distribution of polarized intensities and its centro-symmetric polarization pattern in the outer part are the same with the previous imaging observation by Lucas et al. (2004) and Murakawa et al. (2008) using CIAO. They observed high polarized intensities around 50% at the north-eastern lobe which were well reproduced in our observations.

The same kind of observations using the adaptive optics has not been conducted with the limited engineering time (before 2009 Aug). However, this example just demonstrates how the HiCIAO polarimetry works well at the Nasmyth platform.

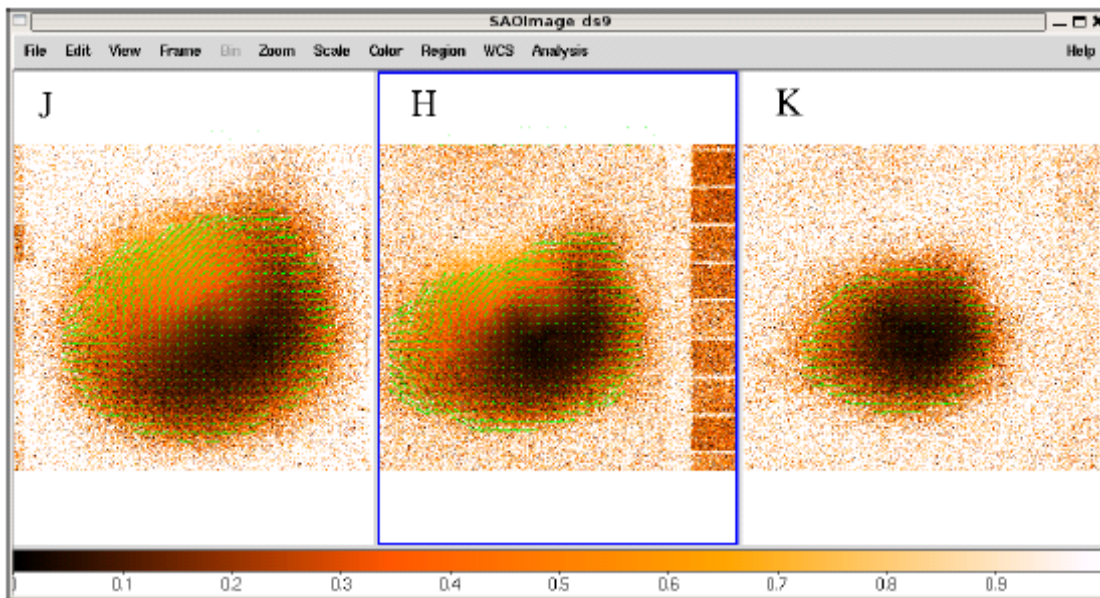


Figure 8.1: The polarized intensity images overlaid with polarization vector maps (HL Tau).

8.3.2 DoAr 21

We also observed DoAr21 in the rho Ophiuchi star forming region on 2009 August 3 for the same aim with HL Tau. Since the seeing was good and stable, adaptive optics allowed us to observe in a high spatial resolution $\sim 0.06''$ in the H band. We took 4 frames of $100 \text{ s} \times 1$ co-adds integration per waveplate position (0° , 22.5° , 45° , and 67.5°). Observation procedure and data reductions for DoAr21 are the same as with those of HL Tau. Since we used pinhole

images for correcting the geometrical distortion, the positional accuracy of the split two images are within ~ 0.1 pixels. DoAr21 has a transitional disk which has optically thin inner regions but optically thick outer ones (Salyk et al. 2009). The observed polarization vectors are aligned at $\sim 45^\circ$ in Fig. 8.2. This is probably due to either (1) remaining instrumental polarization or (2) interstellar polarization. Whatever the case, the point here is that we can measure the polarization close to the central star and till the edge of the occulting mask in the dual beam mode of HiCIAO.

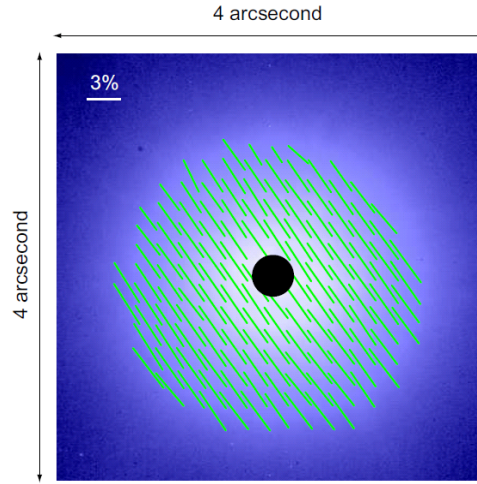


Figure 8.2: The H band polarization vectors are superposed on intensity image (DoAr21).

9. Impact of performance on planet and disk detection

The performance in the SEEDS proposal was based on the "predicted" specification. However, the "real" HiCIAO+AO188 performance might affect the planet discovery space discussed in the proposal. Therefore, in this section we will discuss the impact of the real performance of HiCIAO on the telescope. In summary, the current HiCIAO performance does not significantly change our claim on the planet/disk detection described in the proposal.

We have re-calculated the detectable planets in the following four cases, assuming the most significant factors are the achieved contrast and sensitivities:

- 1) The same specification (contrast, sensitivity) in the CDR document.
- 2) The same contrast, but 0.38 mag worse sensitivity (e.g., a half efficiency).
- 3) The same sensitivity, but 1 order worse contrast (e.g., fainter guide stars).
- 4) One order worse contrast and 0.38 mag worse sensitivity.

In fact, the HiCIAO sensitivities are high enough for any planet detections, and only 0.38 mag (even maximum of ~ 2 mag) worse sensitivity from the original estimate is not a problem for young planet detection. Therefore, the planet detection is solely determined by the contrast limit in HiCIAO.

The resulting planet detection parameter spaces (in masses and radial distances) are shown in Figures 9.1-9.4.

The calculation details are described below. Note we used 0.2" mask here but the commissioning observations were made with 0.3" mask.

The following three conditions must be simultaneously satisfied for directly detection of light emitted by an exoplanet with HiCIAO:

1. The exoplanet is not hidden by the occulting masks.
2. The planet flux lies above 5σ point source detection limit.
(The planet flux can be detected at 5σ level.)
3. The flux of the planet is brighter than stellar halo suppressed by the coronagraph mask.

The inner edge of the region where planets can be detected with HiCIAO is determined by the first condition. When Taurus star formation region at 140pc is observed with the coronagraph mask of 0.2" diameter, the minimum semi-major axis of the region where planets can be detected is 14AU. On the other hand, in the case of nearby stars at 10pc, the semi-major axis of the inner edge is 1AU. Next, the second condition leads us to derive the minimum mass of the planets, whose fluxes can be detected with HiCIAO at 5σ level. The planet flux depends on the age and planet mass. The "original" point source detection limits for each band of HiCIAO can be found in Table 1.1. Table 9.1 shows the expected H band absolute magnitude of the self-luminous planet as the function of the age and planet mass (Baraffe et al. 2003). The red dashed line in each figure show the detection limit determined by the second condition. Finally, the third condition is consistent with a matter that the planet-to-star flux ratio at H band is smaller than the contrast performance of HiCIAO. The detection limit is calculated from the expected stellar flux based on Baraffe et al. (1998). The solid lines in each figure show the third condition.

Table 9.1 : H band absolute magnitude of self-luminous planets.

	10Myr	100Myr	500Myr	1Gyr
1M _J	17.8	22.4	29.2	32.1
5M _J	13.2	17	20.1	22
10M _J	11.3	14.9	17.7	19.1

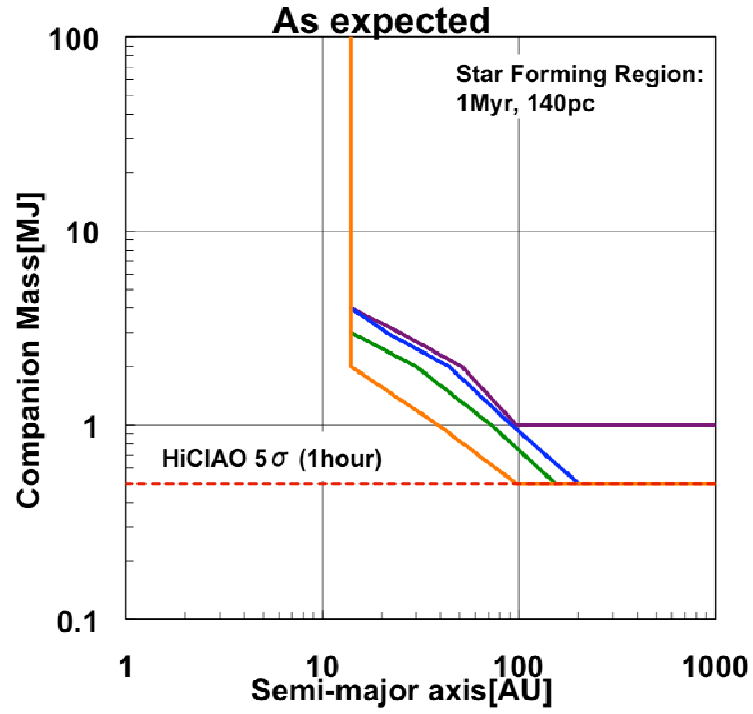


Fig. 9.1. Detection limit of HiCIAO around stars of various masses at Taurus Star Forming Region (1Myr, 140pc) in the case of the expected performance. Purple: $1.4M_{\text{sun}}$, Blue: $1.0M_{\text{sun}}$, Green: $0.6M_{\text{sun}}$, Orange: $0.4M_{\text{sun}}$.

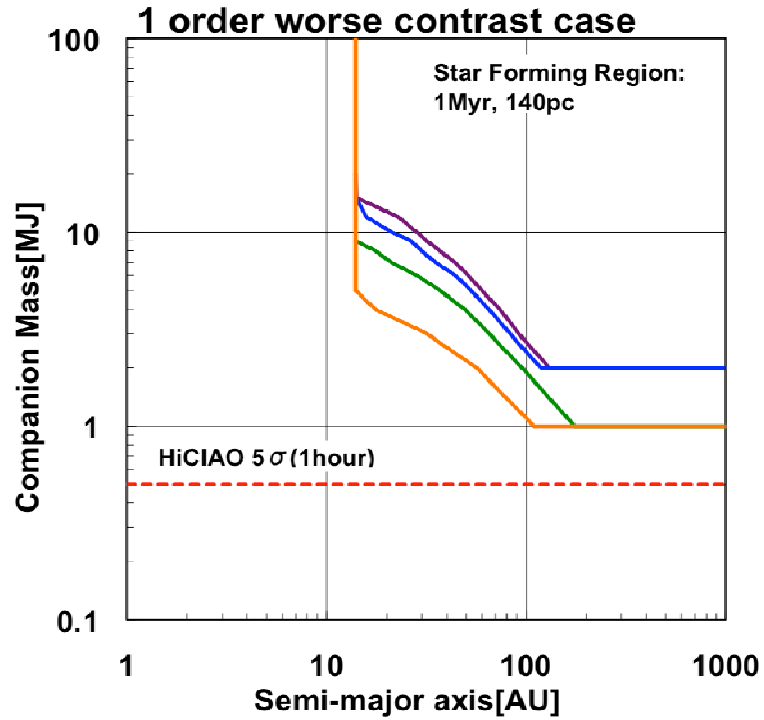


Fig. 9.2. Detection limit of HiCIAO around stars of various masses at Taurus Star Forming Region (1Myr, 140pc) in the case of 1 order worse contrast.

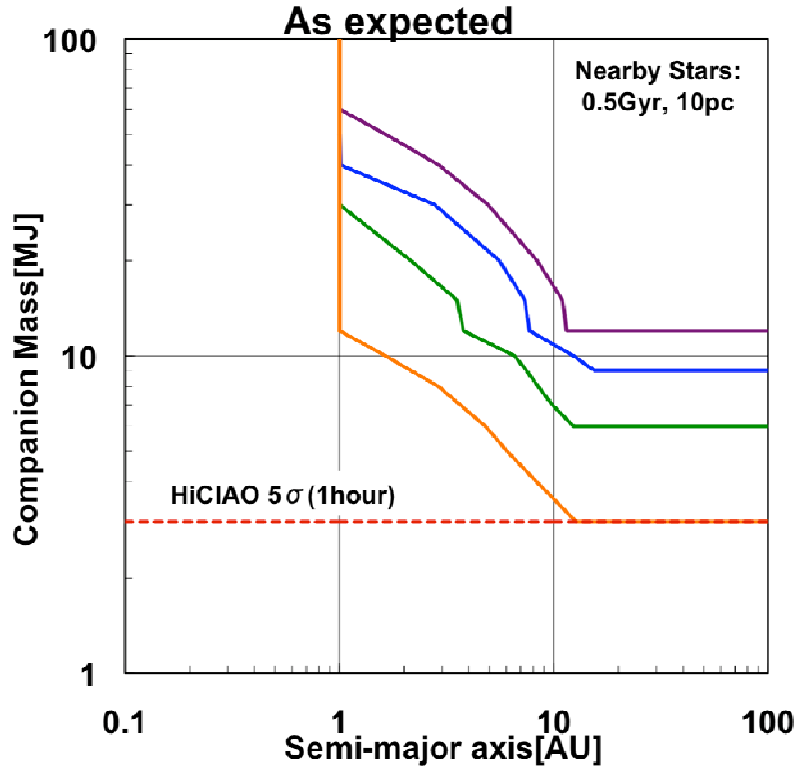


Fig. 9.3. Detection limit of HiCIAO around $1M_{\text{sun}}$ star with 0.5 Gyr at 10pc in the case of the expected performance.

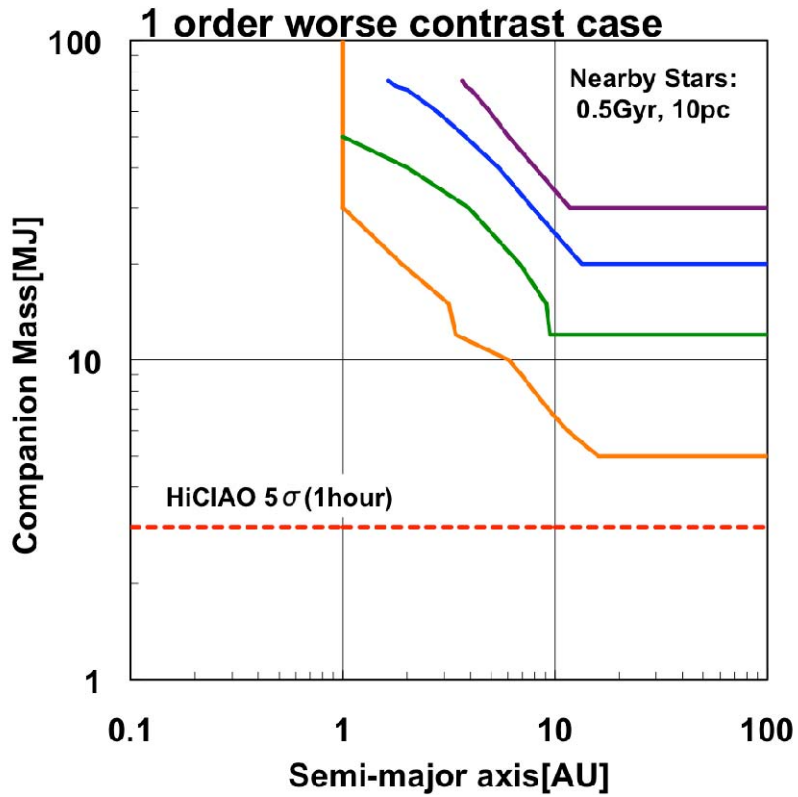


Fig. 9.4. Detection limit of HiCIAO around $1M_{\text{sun}}$ star with 0.5 Gyr at 10pc in the case of 1 order worse contrast.

Appendix 1: Contrast summary (5 σ , 1hr)

We show a quick tabular summary of the HiCIAO contrast values below. The DI mode values with the self-subtraction and the CIAO values are just for a reference.

MASKS/ MODES	0.15"	0.3"	0.5"	1"	1.2"	1.5"
DI (H)	---	(-4.14)	(-4.51)	(-5.46)	(-5.7)	(-6.09)
DI (K)	---	(-4.45)	(-4.62)	(-5.60)	(-5.7)	(-6.09)
SDI (H)	-3.94	-4.26	-4.65	-5.32	-5.42	---
ADI (H)	---	-3.7	-4.3	-5.4	-5.6	-6.0
ADI (K)	---	-4.3	-4.7	-5.5	-5.7	-6.0
PDI (H)	-4.0	-4.6	-4.8	-5.8	-6.0	-6.1
CS(H)	-3.70	-4.0	-4.5	-5.2	-5.4	\sim -5.7
CIAO(K)	---	---	---	---	-4.3	\sim -4.7

Notes:

DI=direct imaging mode

SDI=spectral differential imaging mode

ADI=angular differential imaging mode

PDI=polarization differential imaging mode

CS=computer simulation including AO and coronagraph performances

CIAO=previous coronagraph performance

Also note that these contrast values are measured under different seeing conditions and different central star brightness, although the latter is bright enough for nearly constant Strehl ratio. Therefore, the above table should be regarded as a quick look comparison rather than a performance competition among various modes.

PDI contrast is based on the subtraction of two images with the same filter; so the chromatic aberration is expected to be minimal and its contrast is excellent.

During the DI mode test, the seeing condition seems to be exceptionally stable. Therefore, DI mode contrast for the short exposure time is good, but one should be cautious to scale to 1hr integration time in the DI mode. In contrast, the other differential imaging modes can improve the signal-to-noise ratio with time.

Appendix 2: Distortion details

A2.1 Distortion

For an accurate registration of several dithered or rotated images, the distortion of the focal plane has to be known. In this section a short description of the used methods and the obtained results for the distortion of HiCIAO are presented.

A2.2 Observations

To measure the distortion of HiCIAO, we observed the globular clusters M5 during the engineering runs in May and M15 in August, respectively. Observations were done for all primary observation modes of HiCIAO, i.e. DI, SDI and PDI mode. For DI mode additionally a second data set was obtained for a position angle offset on-sky of 90°. Including the calibration frames, a total of 13 images were taken for DI mode, 6 for SDI and 8 for PDI mode. Approximately 200 to 300 stars could be extracted with sextractor within the 20x20 arcsec field-of-view in DI mode. This provides enough points to determine the distortion over the entire focal plane of HiCIAO.

A2.3 Method

For the determination of the distortion, several methods were used. The first method is based on analyzing 4 images taken with a 4-point dithering along the x- and y-axis. The dithering width was 100 pixel (~1 arcsec). By measuring the shift of each star, as compared to the average shift of all stars, the derivative of the distortion along the dithering direction can be measured. Combining the data from all 4 dithered images and integrating gives the final distortion map. Unfortunately this method is not sensitive to a rotation of the images with respect to the north direction, as well as to an astigmatic pattern.

The second method used was to compare the positions of the stars in the HiCIAO images to the positions of the same star in an image taken by HST. Assuming that the HST image is free of distortion, or at least corrected for distortion, the HST image serves as the reference image. The difference in the positions of the stars in the two images directly gives the distortion at that point in the HiCIAO image.

As a model function for the distortion map, we used a 2 dimensional polynomial function in the pixel coordinates (x, y) of HiCIAO:

$$D_x(x, y) = a_0 + a_1x + a_2y + a_3x^2 + a_4y^2 + a_5xy + a_6x^2y + a_7xy^2 + a_8x^2y^2 + a_9x^3 + a_{10}y^3 + a_{11}x^2y + a_{12}x^3y^2 + a_{13}xy^3 + a_{14}x^2y^3$$

and

$$D_y(x, y) = b_0 + b_1x + b_2y + b_3x^2 + b_4y^2 + b_5xy + b_6x^2y + b_7xy^2 + b_8x^2y^2 + b_9x^3 + b_{10}y^3 + b_{11}x^2y + b_{12}x^3y^2 + b_{13}xy^3 + b_{14}x^2y^3$$

with the parameters $a_0 \dots a_{14}$ and $b_0 \dots b_{14}$.

In a first step, the HiCIAO images were corrected for flat-field and bad pixels. Then the positions of the stars in the HiCIAO images and the HST image were determined with sextractor. For the dithering method, the derivatives of $D_x(x, y)$ and $D_y(x, y)$ were fitted to the measured shift of the stars between two dithered images. For the method based on the HST image, $D_x(x, y)$ and $D_y(x, y)$ were fitted directly to the measured differences in the positions of the stars in the HiCIAO and HST images. Also for this method, the plate-scale of HiCIAO was fixed to 9.5 mas / pixel.

Comparing the results for the distortion map with those obtained for images with a different position angle offset provides an independent check for consistency.

A2.4 Results

Due to the shortcomings of the dithering method, we eventually decided to rely only on the method based on the HST image for determining the distortion of HiCIAO.

Figure A1 shows the results obtained with this method for a sample image of HiCIAO. The main features in this distortion map are a difference in the plate-scale in x- and y-direction of approximately 3%, a small rotation of around 0.38° and a slight deviation from assumed pixel-scale. Figure A2 shows the residuals between the measured data and the fitted model. The average standard deviation for all HiCIAO images of these residuals is 0.78 pixel. This should be mainly due to the fitting error of the centroids in the HiCIAO images, but seems to be rather large. Figure A3 shows the distortion model plotted on a regular grid for better illustration.

In order to achieve a measure for the quality of the fit, we compared the distortion models obtained for the individual HiCIAO images. The standard deviation of the difference in the distortion map (after fitting) over the full $20'' \times 20''$, obtained with various images, but the same position angle is 0.50 pixel, for different position angles it is 0.70 pixel. The large value of the standard deviation is caused almost entirely by the difference in the distortion patterns in the corners of the images. A closer inspection reveals that this is caused mainly by the lack of stars in the corners of several images.

In the central 1024×1024 pixel, the standard deviation of the difference in the distortion maps is on average 0.10 pixel for images with the same position angle and 0.20 pixel for images with a difference in their position angles of 90° .

Figure A4 shows the difference in the obtained distortion pattern for two images with the same position angle, and for two images with a difference in their position angle of 90° .

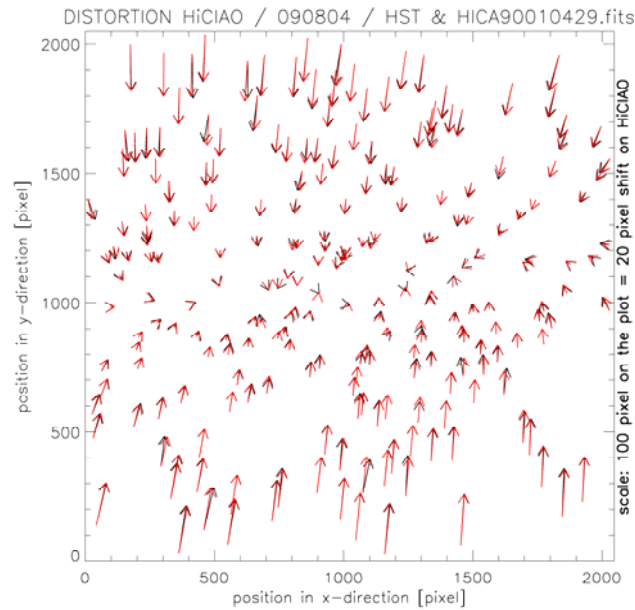


Figure A1. The distortion of HiCIAO in DI mode, as measured with the HST method for a sample image of HiCIAO. Black arrows are the measured shift of the stars between the HiCIAO image and the HST image. Red arrows are the fit of the distortion model to the data.

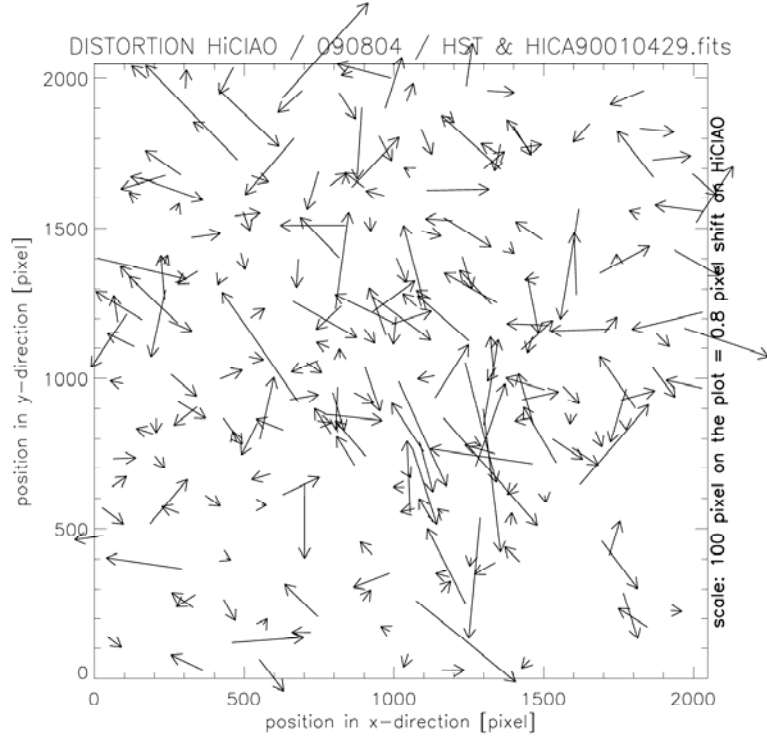


Figure A2. The residuals between the measured shift of the stars and the model function of the data shown in Figure A1.

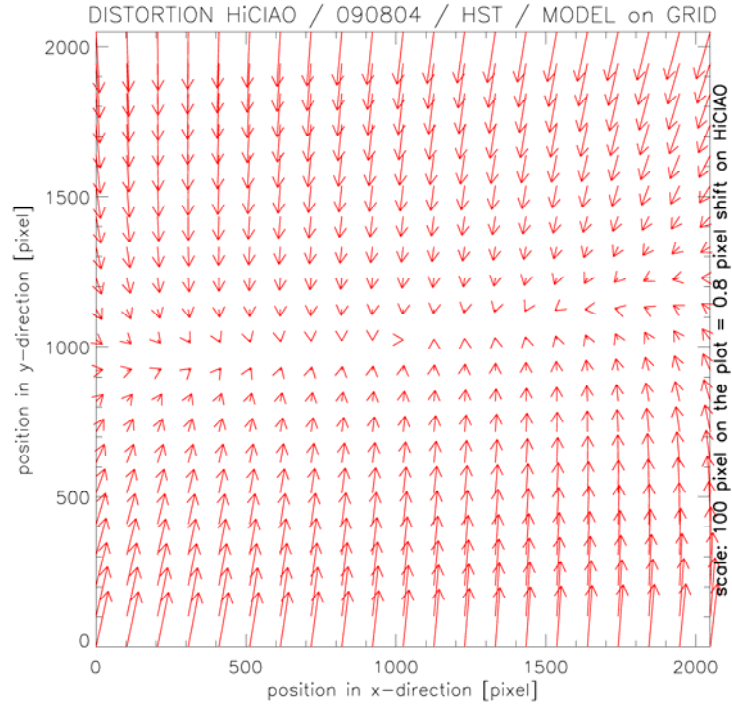


Figure A3. The distortion function obtained above, plotted on a regular grid for better illustration.

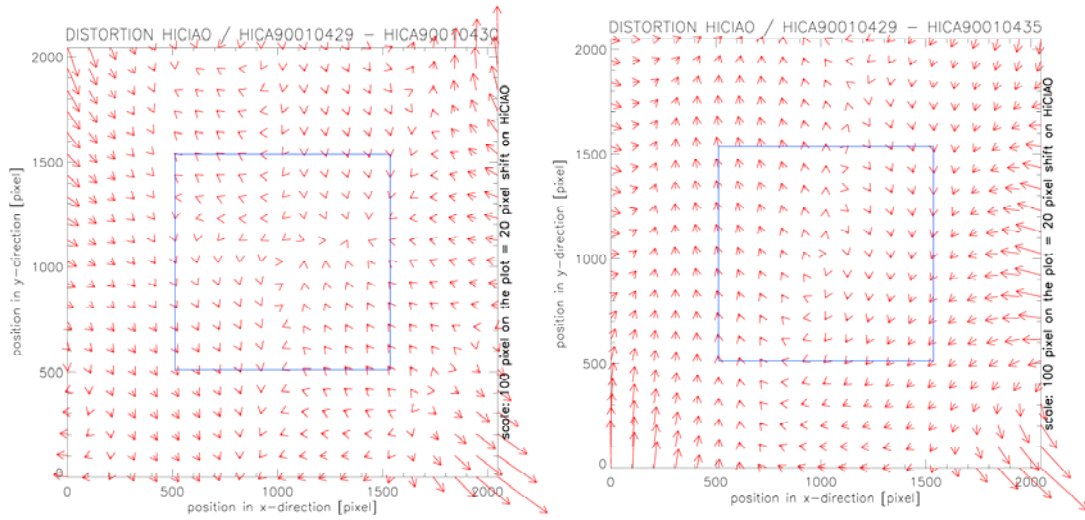


Figure A4. (*Left*): Comparison of the distortion map obtained with two different images of HiCIAO with the same position angle offset. (*Right*): Comparison of the distortion map obtained with two different images of HiCIAO, with a position angle offset of 0° and 90° . In both cases, significant deviations are only present at the corners, where not many stars are available for the fitting.

A2.5 Conclusions

Distortion of the HiCIAO image is analyzed using M15 data. We have used HST data as a distortion-free reference image. Currently available distortion correction algorithm achieves a residual distortion (7 mas rms), which is slightly better than those obtained for two comparable instruments, namely NIRC2 at Keck and PHARO at Palomar (9 mas rms and 19 mas rms, respectively). The result is satisfactory for our purpose. For example, a possible companion to GJ758 was confirmed by a proper motion test, which is 0.1 arcsec in three months (Thalmann et al. 2009, submitted). Relative accuracy of the distortion correction at different position angles is 0.2 pixels in central $10'' \times 10''$ area. This relative accuracy is good enough when images taken in the ADI mode are derotated and registered. As of writing, we have just finished analyzing the distortion in the DI mode, but we will continue the same analysis in the PDI and the SDI mode in future.

REFERECES

- Baraffe, I. 1998, A&A, 337, 403.
- Baraffe, I. 2003, A&A, 402, 701.
- Dupuy, T. J. et al. 2009, ApJ, 692, 729.
- Lafrenière, D. 2007, ApJ, 660, 770.
- Lafrenière, D. et al. 2008, ApJ, 689, L153.
- Lucas, P. W. et al. 2004, MNRAS, 352, 1347.
- Marois, C. et al. 2008, Science, 322, 1348.
- Murakawa, K. et al. 2008, A&A, 492, 731.
- Potter, D. et al. 2002, ApJ, 567, L133.
- Salyk, C. et al. 2009, ApJ, 699, 330.
- Thalmann, C. et al. 2009, submitted
- Whittet, D. C. B. et al. 1992, ApJ, 386, 562.